



# Effective thermo-viscoelastic behavior of short fiber reinforced thermo-rheologically simple polymers: An application to high temperature fiber reinforced additive manufacturing

C.A. Suarez-Afanador, Rémi Cornaggia, Noël Lahellec, Aurelien Maurel-Pantel, Djaffar Boussaa, Hervé Moulinec, Stephane Pierre-Alain Bordas

## ► To cite this version:

C.A. Suarez-Afanador, Rémi Cornaggia, Noël Lahellec, Aurelien Maurel-Pantel, Djaffar Boussaa, et al.. Effective thermo-viscoelastic behavior of short fiber reinforced thermo-rheologically simple polymers: An application to high temperature fiber reinforced additive manufacturing. European Journal of Mechanics - A/Solids, 2022, 96, pp.104701. 10.1016/j.euromechsol.2022.104701 . hal-03698764

**HAL Id: hal-03698764**

**<https://hal.science/hal-03698764>**

Submitted on 28 Nov 2022

**HAL** is a multi-disciplinary open access archive for the deposit and dissemination of scientific research documents, whether they are published or not. The documents may come from teaching and research institutions in France or abroad, or from public or private research centers.

L'archive ouverte pluridisciplinaire **HAL**, est destinée au dépôt et à la diffusion de documents scientifiques de niveau recherche, publiés ou non, émanant des établissements d'enseignement et de recherche français ou étrangers, des laboratoires publics ou privés.

# Effective thermo-viscoelastic behavior of short fiber reinforced thermo-rheologically simple polymers: An application to high temperature fiber reinforced additive manufacturing.\*

C.A. Suarez-Afanador<sup>a,b,\*</sup>, R. Cornaggia<sup>c</sup>, N. Lahellec<sup>a</sup>, A. Maurel-Pantel<sup>a</sup>, D. Boussaa<sup>a</sup>, H. Moulinec<sup>a</sup> and S. P. A. Bordas<sup>b</sup>

<sup>a</sup>Aix-Marseille Université, LMA-CNRS, Centrale Marseille, 4 Impasse Nikola Tesla, 13013 Marseille, France

<sup>b</sup>Université du Luxembourg, Département de mécanique, DSSE, Campus Esch-sur-Alzette, Maison du Nombre, 6 Avenue de la Fonte, L-4364 Esch-sur-Alzette, Luxembourg

<sup>c</sup>Sorbonne Université, CNRS, UMR 7190, Institut Jean Le Rond d'Alembert, F-75005 Paris, France

## ARTICLE INFO

### Keywords:

analytical homogenization  
Full-field FFT homogenization  
thermo-viscoelasticity  
reinforced polymers

## ABSTRACT


This paper presents a procedure for the estimation of the effective thermo-viscoelastic behavior in fiber-reinforced polymer filaments used in high temperature fiber-reinforced additive manufacturing (HT-FRAM). The filament is an amorphous polymer matrix (PEI) reinforced with elastic short glass fibers treated as a single polymer composite (SPC) holding the assumption of thermo-rheologically simple matrix. Effective thermo-viscoelastic behavior is obtained by implementing mean-field homogenization schemes through the extension of the correspondence principle to continuous variations of temperature by using the time-temperature superposition principle and the internal time technique. The state of the fibers in the composite is described through the use of probability distribution functions. Explicit forms of the effective properties are obtained from an identification step, ensuring the same mathematical structure as the matrix behavior. The benchmark simulations are predictions of residual stress resulting from the cooling of the representative elementary volumes (REVs) characterizing the composite filament. The computation of the averaged stress in the benchmarking examples is achieved by solving numerically the stress-strain problem via the internal variables' framework. Reference solutions are obtained from Fast Fourier Transform based full-field homogenization simulations. A comparative analysis is performed, showing the reliability of the proposed homogenization procedure to predict residual stress against extensive computations of the macroscopic behavior of a given microstructure.


## Contents

<b>1</b>	<b>Introduction</b>	<b>2</b>
<b>2</b>	<b>Amorphous polymer matrix behavior</b>	<b>4</b>
2.1	thermo-viscoelasticity under isothermal conditions	4
2.2	thermo-viscoelasticity under non isothermal conditions	6
<b>3</b>	<b>Effective thermo-viscoelastic behavior of the reinforced filament</b>	<b>8</b>
3.1	Short-fibers description	9
3.2	Effective Prony series	12
<b>4</b>	<b>Simulation results</b>	<b>13</b>
4.1	Internal variables' technique for stress computation	13
4.2	Problems setting	14

\*This document is part of a PhD research project funded by the French Ministry of Higher Education, Research and Innovation.

\*Corresponding author

 camilo.suarezafanador@gmail.com (C.A. Suarez-Afanador)

 <http://www.lma.cnrs-mrs.fr/spip/spip.php?auteur373&lang=fr> (C.A. Suarez-Afanador)

ORCID(s): 0000-0002-8816-4848 (C.A. Suarez-Afanador)

4.3 Numerical considerations . . . . .	15
4.4 Comparisons . . . . .	18
<b>5 Conclusions &amp; Perspectives</b>	<b>28</b>
<b>A Mean-field models</b>	<b>29</b>
<b>B Mathematical tools</b>	<b>31</b>
B.1 Transversely isotropic elasticity tensors and matrix representation . . . . .	31
B.2 Products of tensors in Hill basis . . . . .	32
B.3 Orientation averaged Hill basis . . . . .	32
B.4 Orientation tensors for Advani-Tucker law . . . . .	32
<b>C Parameters identification</b>	<b>33</b>
<b>D Materials' data</b>	<b>35</b>

## 1. Introduction

Additive manufacturing (known as 3D-printing) is a booming technology covering a wide range of applications [26, 37]. Fused deposition modeling (FDM) is one of the variations of this technology, based essentially on thermoplastic polymer filament [15]. Transport, medical and sports industries are on the way to integrate the FDM technique to design structural parts, aiming to take advantage of the versatility of the process and looking to achieve the best strength-to-weight ratio. FDM 3D-printing of engineering polymers is able to offer parts with low-scale production, presenting completely adapted solutions for final costumers [18].

The FDM printing process induces a complex thermal history in the thermoplastic filament: from almost the material's melting temperature to room temperature. This severe thermo-mechanical loading creates significant defects in 3D-printed parts, commonly referred as warping [11], due to the creation of residual thermal internal stresses during the cooling of the polymer [50]. Currently, to estimate these internal stresses, finite element methods in commercial codes [29, 28] solve the thermo-mechanical structural problem by integrating thermo-viscoelastic behavior laws for the polymer material [5, 58].

In order to further improve the mechanical strength of the printed parts, fiber-reinforced additive manufacturing (FRAM) has been developed and has the advantage of combining the FDM process with the ability to manufacture a short [22, 49] or continuous fiber composite part [32]. In order to improve the temperature strength of the printed parts, high temperature 3D-printing has been developed and has been naturally extended to fibre-reinforced high temperature thermoplastic polymers in order to obtain parts with good thermomechanical properties [60]. One of the most widely used matrix-materials to address these issues is the polyetherimide (PEI) commercially known as Ultem<sup>®</sup>, which is an amorphous polymer with a good combination of thermal and mechanical properties. The elevated glass transition temperature ( $T_g > 210^\circ\text{C}$ ) of the PEI reflects its high thermal stability, but complicates the control of the printing process in requiring high printing temperatures ( $T_p > 350^\circ\text{C}$ ). The PEI filament reinforced with glass fibers is the material considered in the present work.

With the HT-FRAM 3D-printing process, a composite part is now 3D-printed with a thermal history involving a wide range of temperature, moreover the calculation of the thermo-mechanical behavior becomes multiscale (taking into account the microstructure: length and orientation distribution of glass fibers). The scale characterizing the heterogeneity of the reinforced thermoplastic filament is the scale of glass fibers (around  $100\ \mu\text{m}$  length and  $10\ \mu\text{m}$  diameter) and is much lower than the scale of the printed part (the composite structure of the PEI filament reinforced with glass fibers is observed in using three-dimensional computerized tomography scans (CT-scans) as related in Fig. 1). In consequence, it is no longer possible to use conventional codes based on the finite element method to take into account the effect of the reinforcement on the behavior of the composite filament, as it becomes too expensive to predict.

It is necessary to choose a homogenization method to describe the effective behavior of the fiber-reinforced filament, (see for instance [43]). The macroscopic behavior can be given as a result of numerical simulations in the case of full-field methods (see for instance [44, 45, 17, 9, 8]). In case of complex microstructures, the estimates given by the mean field methods are no longer accurate and require numerical calculations to be approximated (see [42] and [54])

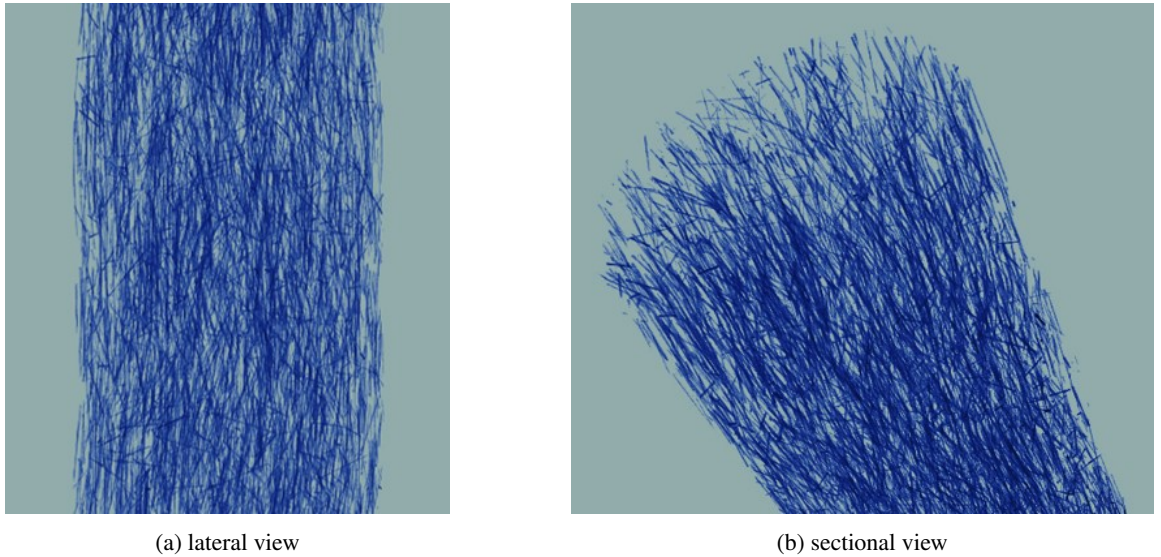


**Figure 1:** 3D reconstruction of CT-scans acquisitions performed on the PEI FDM glass fiber reinforced filament with a volume fraction of 10%. The scanning step used an X-ray source with a voxel size of  $2.67 \mu\text{m}$ , a voltage of 150 kv and a current of  $18 \mu\text{A}$ . The imager has a resolution of  $1920 \times 1536$  pixels. The device used is an EasyTom XL Ultra 150/160 ( $\mu\text{CT}$ ) produced by RX Solution. The pictures describe the volume rendering of fibers embedded in the PEI matrix.

in the case of poly-crystals). Full-field methods can handle a lot of complexities in constitutive laws describing their behavior (non-linearity, plasticity, aging...), but they only give the response of the composite for a particular loading path. This requires a large amount of computations on many REV's (Representative Elementary Volume) with different distributions of inclusions. The cost in terms of calculation time can be too much expensive.

The macroscopic behavior can be also described in an analytical way in the thanks to mean-field methods (see among others [31, 16]). In linear viscoelasticity framework, by using the correspondence principle, several authors like [40] or [52] among others, find some estimates in closed form for the macroscopic behavior of isotropic composites with microstructures following the Hashin-Shtrikman lower bound. Gupta et al. [24] has investigated a Mori-Tanaka (MT) approach to predict the elastic effective properties of a 3D-printed composite material, assuming that the matrix (thermoplastic polymer) and fibers (carbon fiber) are linearly elastic and homogeneous, to predict the elastic effective properties of 3D-printed composite material. Hessman et al. [27] has confronted different mean field homogenization schemes to predict elastic effective properties for short fiber reinforced composites using a fiber length distribution and an orientation distribution in Advani and Tucker form [1]. The authors show that reasonable predictions for effective elastic properties are possible even with limited microstructural information. Muliana [46] has proposed a micromechanical model to predict thermal properties and thermo-viscoelastic response of a functionally graded material idealized as solid spherical particles spatially distributed in a homogeneous matrix. Both constituents are considered thermo-viscoelastic. Although mean-field approximations are more difficult to obtain for complex constituents behaviors, certain non-linearities exhibited by polymer matrices can be accounted for, see the case of an elastoplastic matrix in [35, 7].

The present work proposes to predict the residual thermal internal stresses during the cooling of this HT-FRAM 3D-printed composite in using mean field homogenization technique and correspondence principle to estimate the effective behavior of a thermo-viscoelastic amorphous polymer matrix (PEI) reinforced with a transverse isotropic distribution of the elastic inclusions (short Glass Fibers (GF)). In Section 2, the matrix in which the short glass fibers are embedded is an amorphous polymer assumed to belong to the group of thermo-rheologically simple materials [14]. The polymer follows the time temperature superposition principle (TTS) [3] and the material functions describing its behavior are presented using the notion of "internal time" [25, 13]. The PEI-like matrix thermo-viscoelastic model parameters are identified (and some of them estimated) with the experimental data taken from data-sheet from SABIC [55]. In Section 3, the procedure to perform mean-field homogenization in single polymer composite (SPC) with elastic fibrous reinforcements is presented. Probabilistic description of the Representative Elementary

Volume (REV) and supplementary identification step to ensure the same mathematical structure for the matrix and the composite are presented as well. In Section 4, first, the internal variables' approach to rewrite the local thermo-viscoelastic problem is given, as well as its incremental scheme to update the residual stress. Three different scenarios are considered to compare the accuracy of the presented mean-field homogenization procedure with respect to Fast Fourier Transform (FFT) based full-field homogenization simulations. The reference solutions are computed using REV's that are statistically equivalent to the distribution parameters chosen for the microstructure iterations that are used in the mean-field computations. Convergence studies for the reference solutions are presented as well. Finally, a comparative analysis is performed for each scenario.

## 2. Amorphous polymer matrix behavior

This section presents the thermo-viscoelastic model used to describe the behavior of the PEI-like amorphous polymer. The model is based on the following assumptions: thermo-rheologically simple material [14], time temperature superposition principle (TTS) [3], and the notion of internal time [13, 25]. The model's parameters are identified by using data given by the material supplier SABIC [55], and other supplementary assumptions to circumvent the lack of experimental data (Appendix D).

### 2.1. thermo-viscoelasticity under isothermal conditions

Constitutive equations of the viscoelastic polymer matrix are written under the Boltzmann superposition principle [23, 41], which in the case of a non-aging isotropic viscoelastic solid at equilibrium under isothermal conditions ( $T$  is constant), and stress-free for  $t \leq 0$ , can be represented as follows:

$$\sigma(t) = \int_{-\infty}^t \mathbf{L}(t - \tau, T) d\epsilon(\tau) = \left( \mathbf{L}(\cdot, T) * \frac{d\epsilon}{dt} \right)(t) = (\mathbf{L}(\cdot, T) \otimes \epsilon)(t), \quad (1)$$

with

$$\mathbf{L}(t, T) = 3\kappa(t, T)\mathbf{J} + 2\mu(t, T)\mathbf{K}, \quad (2)$$

where  $T$  is the constant temperature characterizing the thermal state of the polymer,  $\sigma(t)$  and  $\epsilon(t)$  are the stress and infinitesimal strain second-order tensors, respectively. The fourth-order relaxation tensor of the isotropic matrix  $\mathbf{L}(t, T)$ , is characterized by  $\kappa(t, T)$  and  $\mu(t, T)$ , the compressibility and shear relaxation modulus respectively, and  $\mathbf{J}$  and  $\mathbf{K}$ , the hydrostatic and deviatoric fourth-order projectors respectively [51]. Symbols  $*$  and  $\otimes$  denotes classical and Stieltjes convolution product [41]. The dependence of  $\mathbf{L}(t, T)$  on the given temperature  $T$  at which some experiment is performed is represented via the time-temperature superposition principle of thermorheologically simple materials [36, 20], which define  $\mathbf{L}(t, T)$  as

$$\mathbf{L}(t, T) = \mathbf{L}\left(\frac{t}{a_T(T)}\right), \quad (3)$$

where  $a_T(T)$  is the shift factor function, which enables the description of the properties at multiple constant temperature states from a single reference curve of the property, known as master-curve, obtained for a chosen reference temperature  $T_r$  for which  $a_T(T_r) = 1$ . In practice, this is reflected in a horizontal displacement in the plot of the observed property as a function of the logarithmic time or frequency (Fig. 2). The isotropic relaxation moduli,  $\kappa$  and  $\mu$ , are represented by using the following Generalized Maxwell model (or Prony series model) [23, 25, 56]:

$$\mathbf{L}\left(\frac{t}{a_T(T)}\right) = 3\left[\kappa_g - \sum_{u=1}^U \kappa^{(u)}\left(1 - \exp\left(\frac{-t}{a_T(T)\tau_L^{(u)}}\right)\right)\right]\mathbf{J} + 2\left[\mu_g - \sum_{u=1}^U \mu^{(u)}\left(1 - \exp\left(\frac{-t}{a_T(T)\tau_L^{(u)}}\right)\right)\right]\mathbf{K}, \quad (4)$$

where  $\kappa_g = \kappa_\infty + \sum_{u=1}^U \kappa^{(u)}$  and  $\mu_g = \mu_\infty + \sum_{u=1}^U \mu^{(u)}$  are the compressibility and shear glassy modulus respectively, assumed to be temperature independent,  $U$  is the number of Maxwell branches,  $\kappa^{(u)}$  and  $\mu^{(u)}$  and  $\tau_L^{(u)}$  are the coefficients and relaxation time associated with each branch  $u$ . Fig. 3a shows the moduli  $\kappa^{(u)}$  and  $\mu^{(u)}$  for the different relaxation times  $\tau_L^{(u)}$ . Fig. 3b shows the evolution of the relaxation moduli  $\kappa$  and  $\mu$  with respect to time at the reference temperature.

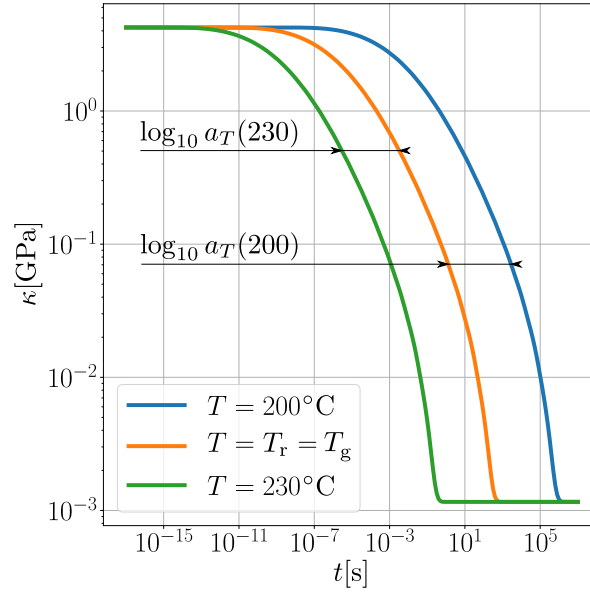
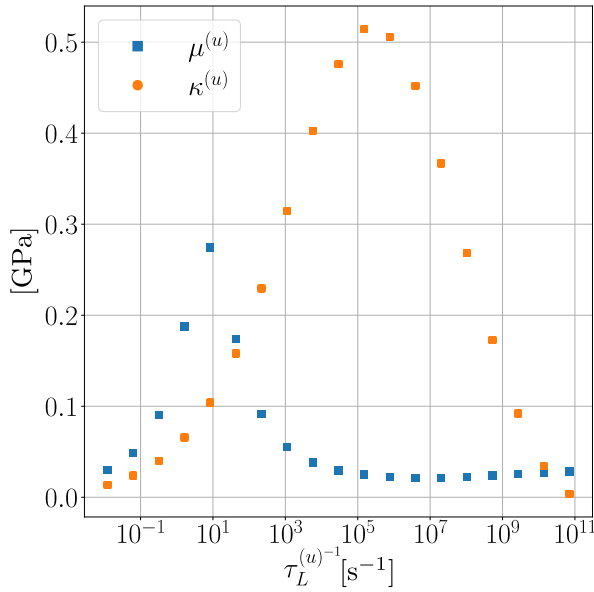
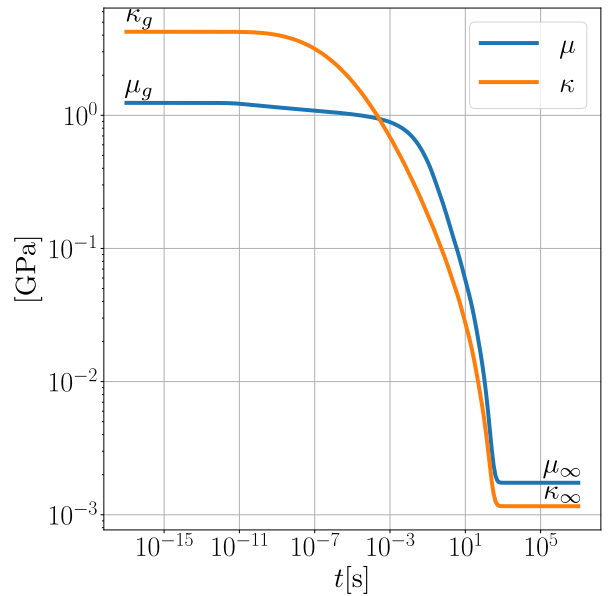


**Figure 2:** Time-temperature superposition in compressibility modulus.



(a) Moduli distributions with shared characteristic times  $\tau_L^{(u)}$ .



(b) Relaxation moduli vs. time.

**Figure 3:** Relaxation spectra characterizing the linear viscoelastic behavior of a PEI-like polymer matrix used in the present work.

The explicit form of the shift factor function  $a_T$  for polymers varies in literature with the range of temperature of the observed material [57]. The most widely used formulations are the WLF (Williams-Landel-Ferry [20]) commonly used for temperatures above the glass transition, the VFTH (Vogel-Fulcher-Tamman-Hesse) equation, and the Arrhenius equation for terminal flow [57]. In view of the experimental results available on PEI matrix of the 3D-printed filament,

it was found that, the best one is the model VFTH which define the  $a_T$  function as follows:

$$\log_{10} a_T(T) = a + \frac{b}{c + (T - T_r)}, \quad (5)$$

with  $a$ ,  $b$  and  $c$ , three material parameters. This function is implemented in the whole characteristic range of temperature with piecewise constant coefficients (with  $T_s$  characterizing the discontinuity) from either side of the glass transition temperature  $T_g = T_r = 216^\circ\text{C}$ , which give the evolution plotted on Fig. 4. Numerical values of the material parameters are shown in Table. 1.

**Table 1**  
Piecewise constant coefficients of the VFTH function

$T_s = 205.099$	$T < T_s$	$T > T_s$
$a$	-3.56811	-17.0449
$b$	1882.297	1129.382
$c$	288.3494	66.36251

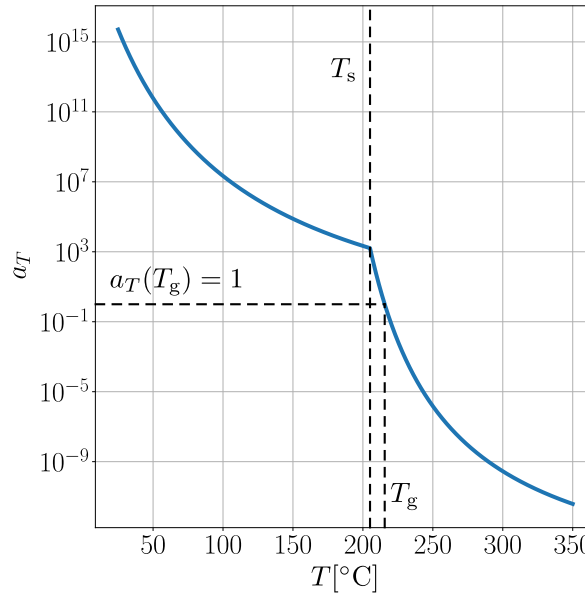


**Figure 4:** VFTH shift function with piecewise constant coefficients.

## 2.2. thermo-viscoelasticity under non isothermal conditions

HT-FRAM 3D-printing process implies continuous variations of the temperature as a function of time, which modify the stiffness of the material and its free volume. Following [13], the constitutive relation (1) can be extended to non-isothermal loading by using the internal time  $\xi$  as the time variable replacing the observer's time  $t$  and which depends on the temperature history through the following relationship:

$$\xi(t) = \int_0^t \frac{du}{a_T(T(u))}. \quad (6)$$



Computed internal times for given linear cooling histories at different rates is presented in Fig. 5a. With the definition (6) of the internal time  $\xi$ , and recalling that all the quantities of interest are now defined in the internal time domain,  $\xi$ , to preserve the convolution interpretation of the integrals in the constitutive equations. The stress-strain equation (Eq. 1) under non-isothermal conditions reads

$$\sigma(\xi) = \int_{-\infty}^{\xi} \mathbf{L}(\xi - v) (\dot{\epsilon}(v) - \dot{\beta}(v)) dv = (\mathbf{L} \otimes (\epsilon - \beta))(\xi). \quad (7)$$

In Eq. (7),  $\beta$  is the thermal strain tensor defined by:

$$\beta(\xi) = \int_{-\infty}^{\xi} \alpha(\xi - v) d\theta(v) \quad \text{and} \quad \alpha(\xi) = \left[ \alpha_1 - \sum_{s=1}^S \alpha^{(s)} \exp\left(\frac{-\xi}{\tau_\alpha^{(s)}}\right) \right] \mathbf{I}_2, \quad (8)$$

where  $\alpha(\xi)$  is the thermal creep function,  $\theta(\xi) = T(\xi) - T_0$ , is the change of temperature from the initial temperature  $T_0$ ,  $\mathbf{I}_2$  is the second order identity tensor,  $\alpha_1$  the high temperature thermal expansion coefficient ( $T > T_g$ ),  $\alpha_g = \alpha_1 - \sum_{s=1}^S \alpha^{(s)}$  the low temperature thermal expansion coefficient ( $T < T_g$ ), and  $\alpha^{(s)}$  and  $\tau_\alpha^{(s)}$  are the thermal expansion coefficients and relaxation times, characterizing the time dependence of the thermal strain. This representation of the polymer's thermal strain has been used in [48, 12] to predict thermo-mechanical behavior in shape memory polymers, and in [33] to predict volume shrinkage in quenching experiments in PVAc samples. As expected from the conclusions of A. J. Kovacs in [34], this approach allows a more complete description of the evolution of the structural state of the polymer. This model is able to take into account the dependence of the volume variations in function of the rate of temperature change [33]. It must be noted that  $\alpha(\xi)$  is defined in the internal time domain, reflecting the fact that thermal expansion properties are affected by temperature in the same way as the mechanical properties. Moreover, this spectral form of the dilatation coefficient appears naturally in the thermo-viscoelastic effective behavior of the composite even when the matrix expansion coefficient is assumed to be constant in function of time. In Fig. 5b, computed matrix' thermal dilatation are shown for various linear cooling histories.

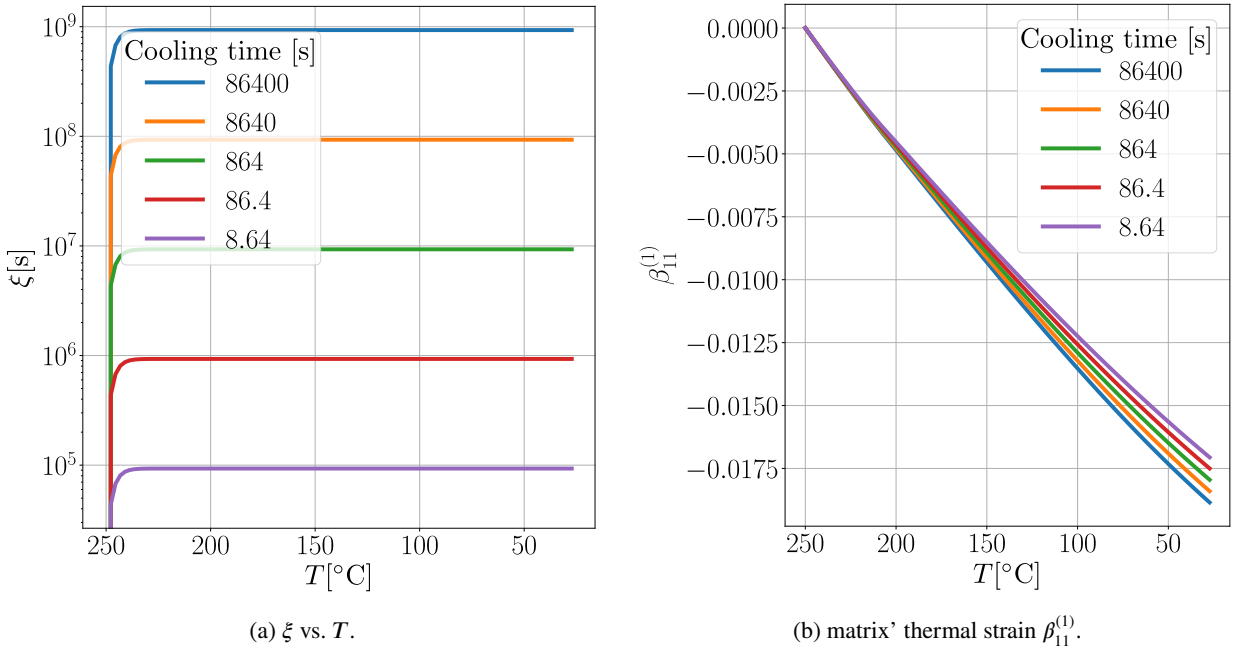


**Figure 5:** Computed internal time and thermal strains of the amorphous polymer matrix, identified with a superscript (1) (i.e.  $\{\cdot\}^{(1)}$ ) for various linear cooling rates.



### 3. Effective thermo-viscoelastic behavior of the reinforced filament

This section presents the mean-field homogenization procedure. The objective is to give an estimation of the macroscopic stress,  $\bar{\sigma}$ , for given histories of the macroscopic, strain and temperature,  $\bar{\epsilon}$  and  $\bar{T}$  respectively, and for a given Representative Elementary Volume,  $\Omega$ . To do so, we extend the well-known correspondence principle [52, 41, 56, 25, 23] to thermo-mechanical loading by using the fact that, in our case, all the materials constituting the REV share the same internal time  $\xi$ . This property is verified under the following assumptions: i) In the considered REV, only the matrix is thermo-viscoelastic, the fibers are purely elastic and therefore time-independent. ii) The matrix is thermo-rheologically simple, with its behavior given by the equations (7) and (8). iii) For coupled thermo-mechanical homogenization problem, at the REV scale, the mechanical problem have to be solved by considering a homogeneous temperature field  $\bar{T}$  which is the average in the REV of the temperature field  $T(\mathbf{x})$  solving the heat equation in the REV, i.e.  $\bar{T} = \langle T(\mathbf{x}) \rangle = \frac{1}{|\Omega|} \int_{\Omega} T(\mathbf{x}) d\Omega$ . This had been demonstrated by [62] for periodic composites by using asymptotic homogenization in the framework of thermo-viscoelasticity. The effective thermo-viscoelastic response to a thermo-mechanical loading is then given by:  $\bar{\sigma}(\xi) = \langle \sigma(\mathbf{x}, \xi) \rangle$ , with  $\sigma(\mathbf{x}, \xi)$  solving the following equations in  $\Omega$ :

$$\begin{cases} \operatorname{div} \sigma(\mathbf{x}, \xi) &= \mathbf{0} & \forall \mathbf{x} \in \Omega, \\ \sigma(\mathbf{x}, \xi) &= (\mathbf{L}^{(r)} \otimes (\epsilon(\mathbf{x}, \cdot) - \beta^{(r)}))(\xi) & \forall \mathbf{x} \in \Omega^{(r)}, \\ \beta^{(r)}(\xi) &= (\alpha^{(r)} \otimes \bar{\theta})(\xi), \\ \langle \epsilon(\mathbf{x}, \xi) \rangle &= \bar{\epsilon}(\xi), \end{cases} \quad (9)$$

with  $\Omega^{(r)}$  being the volume occupied by phase  $r$  in the REV ( $\Omega = \cup_{r=1}^R \Omega^{(r)}$ ). Boundary conditions and compatibility conditions on  $\epsilon$  must complete this problem. The implementation of mean-field schemes is achieved by using the correspondence principle [41, 25], that utilizes the Laplace-Carson transform to rewrite (9) as a symbolic equivalent of a linear thermoelastic composite. The explicit form of the Laplace-Carson transform ( $\mathcal{LC}\{\cdot\}$ ) is defined as follows:

$$f^*(p) = \mathcal{LC}\{f\}(p) = p\mathcal{L}\{f\}(p) = p \int_0^\infty f(\xi) e^{-p\xi} d\xi, \quad (10)$$

and recalling the property for the Stieltjes convolution product  $f \otimes g$ ,

$$\mathcal{LC}\{f \otimes g\}(p) = p\mathcal{L}\{f\}(p)p\mathcal{L}\{g\}(p) = f^*(p)g^*(p). \quad (11)$$

All the mechanical quantities in (9) are defined in terms of the internal time domain, ensuring the applicability of the property in Eq. (11) to the constitutive equations in (9), and therefore showing the fact that the TTS principle definitions for an SPC filament will remain the same as the matrix. In the Laplace domain, the symbolic homogenization problem reads

$$\begin{cases} \operatorname{div} \sigma^*(\mathbf{x}, p) &= \mathbf{0} & \forall \mathbf{x} \in \Omega, \\ \sigma^*(\mathbf{x}, p) &= \mathbf{L}^{*(r)}(p) : (\epsilon^*(\mathbf{x}, p) - \beta^{*(r)}(p)) & \forall \mathbf{x} \in \Omega^{(r)}, \\ \beta^{*(r)}(p) &= \alpha^{*(r)}(p)\bar{\theta}^*(p) & \forall \mathbf{x} \in \Omega^{(r)}, \\ \langle \epsilon^*(\mathbf{x}, p) \rangle &= \bar{\epsilon}^*(p), \end{cases} \quad (12)$$

with compatibility and boundary conditions.

Based on the theory of effective moduli [6, 61], an approximated solution of the linear problem in (12) is sought using mean-field approaches, that are widely applied to randomly distributed microstructures [27, 4, 39, 63, 19, 53]. In this context, localization tensors ( $\mathbf{A}^{*(r)}(p)$  and  $\mathbf{a}^{*(r)}(p)$ ) are characterized as linear operators relating the local strain of a given phase  $r$  of volume fraction  $c^{(r)}$ , and the macroscopic strain imposed on the REV by assuming strain fields that are uniform per phase ( $\epsilon^*(\mathbf{x}, p) = \mathbf{A}^{*(r)}(p) : \bar{\epsilon}^*(p) + \mathbf{a}^{*(r)}(p)\bar{\theta}^*(p)$ ). By considering the relation given in [61] between the concentration tensors  $\mathbf{A}^{*(r)}(p)$  and  $\mathbf{a}^{*(r)}(p)$ , the effective behavior ( $\tilde{\mathbf{L}}^*(p)$ ,  $\tilde{\alpha}^*(p)$ ) of an R-phases composite in the Laplace-Carson domain is obtained through the following relationships, noting that, in order to lighten the writing, the dependency on the complex variable  $p$  of every transformed quantity is not presented explicitly, but it can be understood in every starred variable,  $\{\cdot\}^*$ .

$$\bar{\sigma}^* = \tilde{L}^* : (\bar{\epsilon}^* - \tilde{\alpha}^* \bar{\theta}^*), \quad (13)$$

with

$$\begin{aligned} \tilde{L}^* &= \left( L^{*(1)} + \sum_{r=2}^R c^{(r)} (L^{*(r)} - L^{*(1)}) : A^{*(r)} \right), \text{ and} \\ \tilde{\alpha}^* &= (\tilde{L}^*)^{-1} : \left( L^{*(1)} : \alpha^{*(1)} + \sum_{r=2}^R c^{(r)} (A^{*(r)})^T : (L^{*(r)} : \alpha^{*(r)} - L^{*(1)} : \alpha^{*(1)}) \right), \end{aligned} \quad (14)$$

where the superscript  $(1)$  denotes the matrix. Three mean-field schemes are implemented: Mori–Tanaka, Lielens and IDD (Interaction Direct Derivative), each of them with a particular form of  $A^{*(r)}$ . It must be noted that in the present work, all chosen schemes involve the mean over the phases of some quantities inside its formulation of the localization tensor. Details about the choices made are presented in Appendix A.

### 3.1. Short-fibers description

A microstructure like the one presented in the microtomography in Fig. 1, should be considered as a heterogeneous medium with  $R - 1$  linear thermoelastic phases embedded in a thermo-viscoelastic matrix (each phase corresponds to a family of elastic fibers sharing the same microstructural parameters (i.e. length and orientation)). The fibrous inclusions of the engineering thermoplastic polymers are commonly made of carbon (transverse isotropic) or glass (isotropic). In the next definitions, transverse-isotropic symmetry will be used for both, the inclusions' and matrix' properties, since an isotropic material can be represented in any transverse-isotropic basis with arbitrary orientation vector  $\mathbf{n}$  of the symmetry axis [51]. The chosen 4th order tensor basis is the Hill basis  $\{\mathcal{H}^{(1)}, \dots, \mathcal{H}^{(b)}, \dots, \mathcal{H}^{(6)}\}(\mathbf{n})$  (Appendix B.1). Constitutive equations of the fibrous inclusions (defined in the internal time), denoted by the superscript  $(f)$ , are presented directly in the Laplace-Carson domain as the explicit form of the fibers' properties remains the same after transformation (i.e.  $L^{*(f)} = L^{(f)}$ ,  $\alpha^{*(f)} = \alpha^{(f)}$ ).

$$\begin{aligned} \sigma^{*(f)}(p) &= L^{(f)}(\mathbf{n}) : (\epsilon^*(p) - \beta^*(p)) = \sum_{b=1}^6 l^{(b,f)} \mathcal{H}^{(b)}(\mathbf{n}) : (\epsilon^*(p) - \beta^*(p)), \\ \beta^{*(f)}(p) &= \alpha^{(f)} \theta^*(p) = \left( \alpha_{11}^{(f)} \Theta + \alpha_{33}^{(f)} \mathcal{N} \right) \theta^*(p), \end{aligned} \quad (15)$$

with  $\alpha_{11}^{(f)}$  and  $\alpha_{33}^{(f)}$ , being the transverse and longitudinal fibers' expansion coefficients associated to the second order tensor basis  $\mathcal{N} = \mathbf{n} \otimes \mathbf{n}$  and  $\Theta = \mathbf{I}_2 - \mathcal{N}$  in terms of the orientation vector  $\mathbf{n}$  (Appendix B.1).

#### *Probabilistic approach to account the presence of fibers:*

In the present study, instead of a deterministic description of the fibers, a continuous distributions approach is implemented for the microstructural parameters [1, 27]. To illustrate this, only the effective mechanical behavior ( $\tilde{L}^*$ ) is presented, as it is enough to show the impact of this technique in the thermo-mechanical macroscopic response. Since it is sought a binary representation of the composite (polymer matrix + fibers), the superscript  $(1)$  is substituted by  $(m)$  as the matrix identification character in Eq. (14). The volume fraction of the polymer matrix is then expressed by:  $c^{(1)} = c^{(m)} = 1 - \sum_{r=2}^R c^{(r)} = 1 - c^{(f)}$ . With  $c^{(f)}$  being the fibers' total volume fraction. Then,  $\tilde{L}^*$  from Eq. (14) is rewritten by considering the explicit form of  $L^{*(f)}$  in Eq. (15) to write both, matrix and inclusions' mechanical properties in the fibers' basis.

$$\tilde{L}^* = L^{*(m)} + c^{(f)} \sum_{b=1}^6 (l^{*(b,f)} - l^{*(b,m)}) \sum_{r=2}^R \frac{c^{(r)}}{c^{(f)}} \mathcal{H}^{(b)}(\mathbf{n}^{(r)}) : A^{*(r)}(\mathbf{n}^{(r)}, w^{(r)}). \quad (16)$$

The above presentation is possible because the fiber families differ only in their orientation ( $\mathbf{n}^{(r)}$ ) and length (i.e. aspect ratio  $w^{(r)} = l^{(r)}/d$ ), so their only differences are in the explicit forms of the Hill basis and the localization tensor. Considering as it is shown in [51] for spheroidal inclusions, that the localization tensor of a fiber family with orientation

$\mathbf{n}^{(r)}$  can be written down in the same basis as its mechanical properties ( $\mathbf{A}^{*(r)} = \sum_{b=1}^6 a^{*(r)}(w^{(r)}) \mathbf{H}^{(b)}(\mathbf{n}^{(r)})$ ), and by introducing the relative volume fraction of a family of fibers with respect to the total number of fibers  $c_f^{(r)} = c^{(r)}/c^{(f)}$  (with  $\sum_{r=2}^R c_f^{(r)} = 1$ ), Eq. (16) reads,

$$\begin{aligned} \tilde{\mathbf{L}}^* &= \mathbf{L}^{*(m)} + c^{(f)} \sum_{b=1}^6 (l^{*(b,f)} - l^{*(b,m)}) \sum_{r=2}^R c_f^{(r)} \mathbf{H}^{(b)}(\mathbf{n}^{(r)}) : \sum_{v=1}^6 a^{*(v,r)}(w^{(r)}) \mathbf{H}^{(v)}(\mathbf{n}^{(r)}) \\ &= \mathbf{L}^{*(m)} + c^{(f)} \sum_{b=1}^6 \sum_{v=1}^6 (l^{*(b,f)} - l^{*(b,m)}) \langle a^{*(v,r)}(w^{(r)}) (\mathbf{H}^{(b)}(\mathbf{n}^{(r)}) : \mathbf{H}^{(v)}(\mathbf{n}^{(r)})) \rangle_{\Omega \setminus \Omega^{(m)}}. \end{aligned} \quad (17)$$

The expression between angle brackets in the foregoing equation represents the volume average over the space of orientations and lengths of the concerned quantities. For the case of an REV with a finite number of fibers, Eq. (17) can be computed explicitly in a deterministic way, however this approach limits the number of fibers describing the distribution of the microstructural parameters. As it is mentioned in [1], The most general description of the fibers' state is the probability distribution function, in which it is possible to consider an infinite number of fibers covering in a more accurate way the distribution of parameters in the composite. The probabilistic approach is then introduced as the number of fibers in  $\Omega$  tends to infinity, therefore its microstructural parameters are no longer defined in a discrete way but characterized by a continuous distribution of the observed parameter.

$$\begin{aligned} \langle a^{*(v,r)}(w^{(r)}) (\mathbf{H}^{(b)}(\mathbf{n}^{(r)}) : \mathbf{H}^{(v)}(\mathbf{n}^{(r)})) \rangle_{\Omega \setminus \Omega^{(m)}} &= \frac{1}{|\Omega \setminus \Omega^{(m)}|} \int_{\Omega \setminus \Omega^{(m)}} a^{*(v,r)}(w^{(r)}) (\mathbf{H}^{(b)}(\mathbf{n}^{(r)}) : \mathbf{H}^{(v)}(\mathbf{n}^{(r)})) d\Omega \\ &= \int_{w_{min}}^{w_{max}} f_w(w) a^{*(v)}(w) dw \int_S f_n(\mathbf{n}) (\mathbf{H}^{(b)}(\mathbf{n}) : \mathbf{H}^{(v)}(\mathbf{n})) dS. \end{aligned} \quad (18)$$

The mean over the distribution of lengths is characterized by the integral of the normalized distribution function ( $f_w(w)$ ), that depends on the aspect ratio ( $w = l/d \in [w_{min}, w_{max}]$ ) being a function of the fiber length ( $l \in [l_{min}, l_{max}]$ ) under the hypothesis of constant fibers' diameter ( $d$ ). The mean over the orientations is computed by integrating over the unit sphere ( $S$ ) the distribution function ( $f_n(\mathbf{n})$ ), depending on the unit direction vector ( $\mathbf{n}$ ).

For the simulation examples of the present work, glass fiber inclusions are considered, in consequence  $\mathbf{L}^{*(r)}$  is independent of the orientation vector  $\mathbf{n}$  of the fiber as it is isotropic and can be represented in any arbitrary transverse isotropic basis  $\{\mathbf{H}^{(b)}\}(\mathbf{n})$ , therefore in Eq. (17) only the localization tensor  $\mathbf{A}^{*(r)}(w^{(r)}, \mathbf{n}^{(r)})$  is different for each family of fibers. This fact reduces the computation of the distribution averages to the computation of the mean coefficients  $\{a_{\star}^{*(v,f)}\}$  and associated mean Hill basis tensors  $\{\mathbf{H}_{\star}^{(v,f)}\}$  (Eqs. (B.8) - (B.10)). Considering this, Eq. (17) under the continuous distribution representation (Eq. (18)) reads

$$\begin{aligned} \tilde{\mathbf{L}}^* &= \mathbf{L}^{*(m)} + c^{(f)} (\mathbf{L}^{*(f)} - \mathbf{L}^{*(m)}) : \sum_{v=1}^6 \int_{w_{min}}^{w_{max}} f_w(w) a^{*(v)}(w) dw \int_S f_n(\mathbf{n}) \mathbf{H}^{(v)}(\mathbf{n}) dS \\ &= \mathbf{L}^{*(m)} + c^{(f)} (\mathbf{L}^{*(f)} - \mathbf{L}^{*(m)}) : \sum_{v=1}^6 a_{\star}^{*(v,f)} \mathbf{H}_{\star}^{(v,f)} = \mathbf{L}^{*(m)} + c^{(f)} (\mathbf{L}^{*(f)} - \mathbf{L}^{*(m)}) : \mathbf{A}_{\star}^{*(f)}, \end{aligned} \quad (19)$$

with  $\mathbf{A}_{\star}^{*(f)}$  being the distribution averaged fibers' localization tensor. The two-phases like version of the effective thermo-viscoelastic behavior (Eq. 14) for the case of isotropic linear elastic glass fibers inclusions is given by:

$$\begin{aligned} \tilde{\mathbf{L}}^* &= \mathbf{L}^{*(m)} + c^{(f)} (\mathbf{L}^{*(f)} - \mathbf{L}^{*(m)}) : \mathbf{A}_{\star}^{*(f)}, \\ \tilde{\boldsymbol{\alpha}}^* &= \bar{\boldsymbol{\alpha}} + (\mathbf{S}^{*(f)} - \mathbf{S}^{*(m)})^{-1} : (\tilde{\mathbf{S}}^* - \bar{\mathbf{S}}^*) : (\boldsymbol{\alpha}^{*(f)} - \boldsymbol{\alpha}^{*(m)}), \end{aligned} \quad (20)$$

where  $\tilde{\mathbf{S}}^*$  and  $\bar{\mathbf{S}}^* = c^{(m)} \mathbf{S}^{*(m)} + c^{(f)} \mathbf{S}^{*(f)}$ , are the effective and average, transformed creep moduli tensor ( $\mathbf{S}^* = (\mathbf{L}^*)^{-1}$ ) respectively.  $\boldsymbol{\alpha}^{*(m)}$ ,  $\boldsymbol{\alpha}^{*(f)}$ , are the matrix' and fibers' thermal expansion second order tensors, respectively. The second equation in Eq. (20) is equivalent to the well-known Levin's equation (Hashin-Rosen, [38, 53]). The choices made for the explicit form of  $f_w(w)$  and  $f_n(\mathbf{n})$  are presented below.

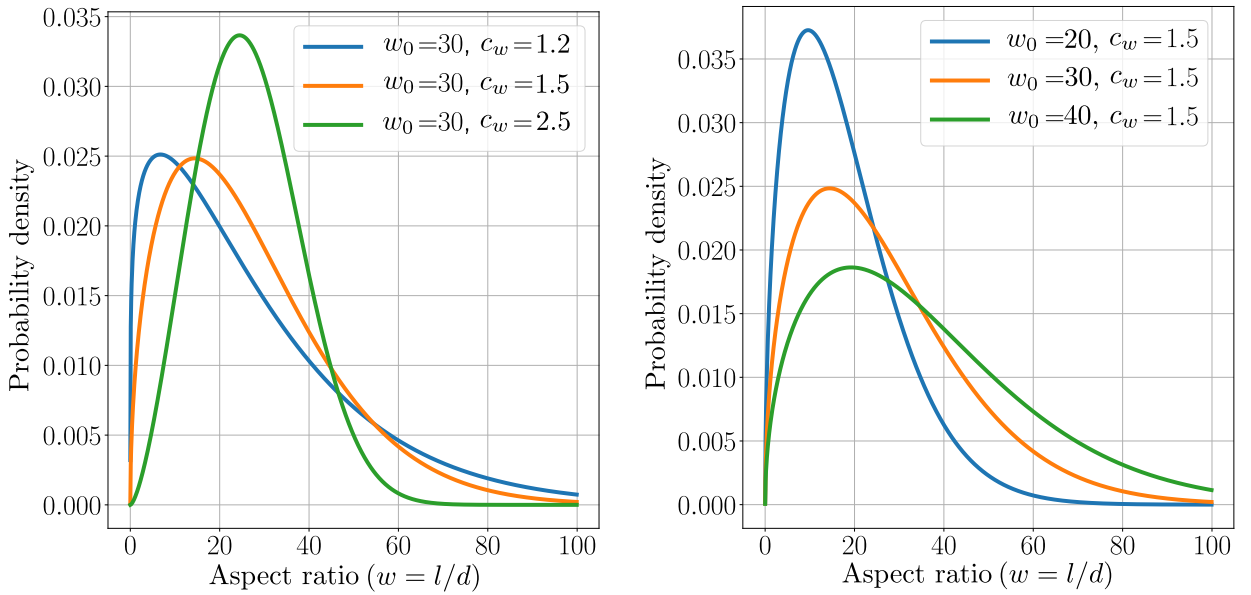
**Weibull's law for length distributions:**

The chosen length probability density function ( $f_w(w)$ ) is the Weibull's law, used in the literature in the context of injection molding thermoplastic composites, where it was demonstrated its accuracy compared to the deterministic approach [47]. The explicit form of the function reads

$$f_w(w) = W(wp(w)), \text{ with}$$

$$p(w) = \frac{c_w}{w_0} \left( \frac{w}{w_0} \right)^{c_w-1} e^{-\left( \frac{w}{w_0} \right)^{c_w}}, \text{ and } W = \left( \int_{w_{min}}^{w_{max}} wp(w)dw \right)^{-1}, \quad (21)$$

where  $c_w$ ,  $w_0$  are the Weibull's law parameters to be fitted from data statistics obtained from image processing (e.g. microtomography Fig. 1). Examples of the parameters range chosen for the present study are presented in Fig. 6. From this figure, it can be noted that the value of  $w_0$  represents the mean aspect ratio. Furthermore, by increasing the value of  $c_w$  at a given  $w_0$  the number of fibers with aspect ratio  $w_0$  is increased.



(a) Probability density plot for a given  $w_0 = 30$  and various  $c_w$  (b) Probability density plot for a given  $c_w = 1.5$  and various  $w_0$ .

**Figure 6:** Weibull's probability density ( $p(w)$ ) plots for various combinations of the parameters ( $c_w$ ,  $w_0$ ) used in the present study.

**Advani and Tucker law for orientation distributions:**

Primal observations of filament microtomography (Fig. 1) suggest an axisymmetric distribution of the fibers' orientation about the filament axis. For this case, the Advani-Tucker's law is proposed in [1] in the context of injection molding composites. In the axisymmetric case, this law is characterized by a single parameter ( $m_{AT}$ ) to be computed from microphotography analysis. The explicit form of the distribution law is presented below.

$$f_n(\theta, \phi) = K \sin^{m_{AT}}(\theta) \cos^{m_{AT}}(\phi), \quad (22)$$

where  $K$  is a normalization constant and,  $\theta$  and  $\phi$  are the direction angles characterizing the orientation deviation of a fiber from the filament axis. The implementation of this approach is simplified by using the mean orientation tensors ( $\eta_2$  and  $\eta_4$ ) as it is done in [1]. This procedure is of particular interest in the case of composites holding material symmetries that enables to write down the effective behavior in a particular choice of basis. Information about the application of the law and computation of orientations tensors can be found in Appendix B.4. Some examples of the orientation distributions used in the present work are presented in Fig. 7. As can be noted from this figure, the number of fibers, oriented in the principal filament's axis direction, increases as  $m_{AT}$  becomes greater. Indeed, the unidirectional case corresponds to the limit  $m_{AT} \rightarrow \infty$ .

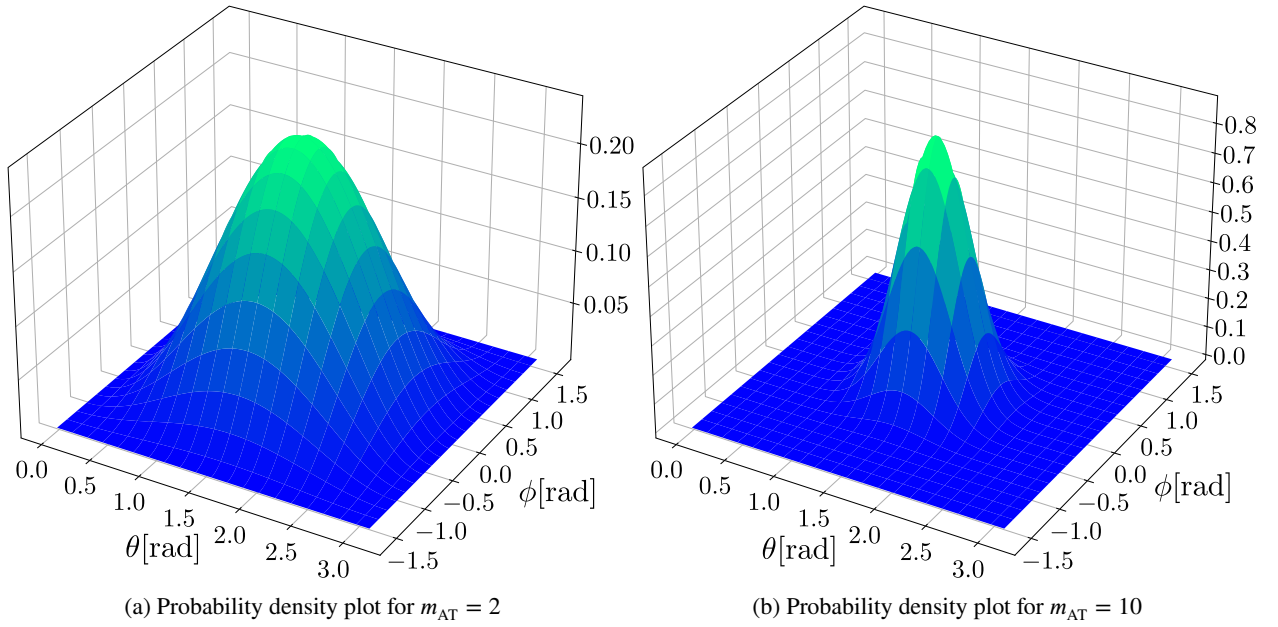


**Figure 7:** Advani-Tucker probability density  $f_n(\mathbf{n})$  for deviation angles  $\theta \in [0, \pi]$  and  $\phi \in [-\pi/2, \pi/2]$

### 3.2. Effective Prony series

To ensure the same mathematical representation of the effective behavior as it was presented for the matrix in the time domain (Prony-series), this study considers a supplementary identification step. In Eq. (20), the effective thermo-viscoelastic behavior is given in the Laplace-Carson domain ( $\tilde{\mathbf{L}}^*$ ,  $\tilde{\boldsymbol{\alpha}}^*$ ). In function of the length of the Prony-series of the polymer matrix and the choice of mean-field scheme, the complexity of the rational polynomials of the elements in  $\tilde{\mathbf{L}}^*$  and  $\tilde{\boldsymbol{\alpha}}^*$  varies, therefore the analytical inversion of the Laplace-Carson transform is sometimes too expensive in terms of computational time or is not giving a sum of weighted exponential functions (Prony-series) as it is desired. Since a complex relaxation moduli tensor  $\mathbf{L}(j\omega)$  is equivalent to the above defined Laplace-Carson transform of the relaxation moduli tensor [21, 25], artificial dynamical mechanical analysis (DMA) is performed, and then processed using KN-HW identification procedure from [30] to obtain an approximation of the discrete spectra (Appendix C). The advantage of this method in contrast with the collocation methods is that it includes an accurate approximation of the characteristic discrete time spectrum. This is performed identically for both, mechanical and thermal Prony-series, differing only on the physical meaning of the identified coefficients. The expected explicit form of  $\tilde{\mathbf{L}}^*$  and  $\tilde{\boldsymbol{\alpha}}^*$  after parameters' identification reads

$$\tilde{\mathbf{L}}^* = \tilde{\mathbf{L}}_g - \sum_{b=1}^6 \sum_{n_b=1}^{N_b} \frac{\tilde{l}^{(b,n_b)}/\tau_L^{(n_b)}}{p + (\tau_L^{(n_b)})^{-1}} \mathbf{H}_{\star}^{(b)}, \quad (23)$$

$$\tilde{\boldsymbol{\alpha}}^* = \tilde{\boldsymbol{\alpha}}_g + \sum_{m=1}^M \frac{\tilde{\alpha}_{11}^{(m)}/\tau_{\alpha}^{(m)}}{p + (\tau_{\alpha}^{(m)})^{-1}} \boldsymbol{\Theta}_{\star} + \sum_{o=1}^O \frac{\tilde{\alpha}_{33}^{(o)}/\tau_{\alpha}^{(o)}}{p + (\tau_{\alpha}^{(o)})^{-1}} \mathcal{N}_{\star}. \quad (24)$$

Here,  $\tilde{\mathbf{L}}_g$  is the effective glassy 4th order stiffness tensor,  $\tilde{\boldsymbol{\alpha}}_g$  is the glassy 2nd order thermal expansion tensor,  $\boldsymbol{\Theta}_{\star} = \mathbf{I}_2 - \boldsymbol{\eta}_2$  is the second-order tensor that characterizes the orthogonal behavior,  $\mathcal{N}_{\star} = \boldsymbol{\eta}_2$  is the second-order tensor that characterizes the symmetry axis behavior (Appendix B.3),  $N_b$  is the length of the Prony-series of the relaxation modulus  $\tilde{l}^{*(b)}$ , and,  $M$  and  $O$  are the lengths of the Prony-series of the effective thermal creep functions  $\tilde{\alpha}_{11}^*$  and  $\tilde{\alpha}_{33}^*$ , respectively.

## 4. Simulation results

The modeling of the matrix thermo-viscoelastic behavior for the specific range of temperatures of the 3D-FDM printing have been presented in Section 2, where linear viscoelasticity, time-temperature superposition principle and the internal time technique were introduced. Section 3 presents the methodology to obtain the effective behavior. The homogenization procedure via mean-field schemes is achieved based on the validity of the applicability of the correspondence principle (Laplace-Carson transform) in continuous variations of temperature for thermo-rheologically simple polymers. Mean-field schemes were presented in a general shared formulation, differing only in the form of the localization tensor  $\mathbf{A}^*(\mathbf{n}^{(r)}, \omega^{(r)})$  in function of the chosen scheme (Appendix A). Probabilistic approach to account for the variability of lengths and orientations of the fibers was introduced as a powerful tool able to map distributions over greater spaces and being very simple in terms of implementation. Finally, the methodology to identify the coefficients of the effective properties of the composite was introduced, ensuring that the composite is represented in the same way as the matrix. This Prony-series representation allows applying directly the internal variables' formulation [41, 5, 52] for the incremental scheme in the computation of stress as a function of time and temperature. In this section, the accuracy of the presented methodology will be compared to extensive heterogeneous simulations in computational REVs using the FFT-based full field homogenization method.

### 4.1. Internal variables' technique for stress computation

The stress computation problem can be formulated as follows:

Given  $\tilde{\mathbf{L}}(t)$ ,  $\tilde{\alpha}(t)$ ,  $a_T(T)$ ,  $\tilde{\epsilon}(t)$  and  $\tilde{\theta}(t) = \tilde{T}(t) - \tilde{T}_0$ , compute  $\tilde{\sigma}(t)$ .

First,  $\xi(t)$  is computed by using Eq. (6) in function of  $\tilde{T}(t)$  and the total observation time of the simulation. Then, a simple way to start the procedure to compute the evolution of the macroscopic stress  $\tilde{\sigma}(t)$  is by considering the explicit form of the Laplace-Carson transform of the stress function (Eq. (7)) for the case of a transverse isotropic homogenized material (Eqs. (23) - (24)), noting that, in order to lighten the writing, the implicit form of the thermal strains is conserved, and its computation is treated separately. It must be note that as [52], the following formulation allows a simple and natural definition of the internal variables forms avoiding integral operations, and reducing the formulation to algebraic operations in rational polynomials.

$$\begin{aligned}\tilde{\sigma}^*(p) &= \left( \tilde{\mathbf{L}}_g - \sum_{b=1}^6 \sum_{n_b=1}^{N_b} \frac{\tilde{l}^{(b,n_b)} / \tau_L^{(n_b)}}{p + (\tau_L^{(n_b)})^{-1}} \mathbf{H}_\star^{(b)} \right) : (\tilde{\epsilon}^*(p) - \tilde{\beta}^*(p)) \\ &= \tilde{\sigma}_g^*(p) - \sum_{b=1}^6 \sum_{n_b=1}^{N_b} \tilde{l}^{(b,n_b)} \frac{\mathbf{H}_\star^{(b)} : (\tilde{\epsilon}^*(p) - \tilde{\beta}^*(p))}{\tau_L^{(n_b)} (p + (\tau_L^{(n_b)})^{-1})},\end{aligned}\quad (25)$$

with

$$\begin{aligned}\tilde{\beta}^*(p) &= \left( \tilde{\alpha}_g + \sum_{m=1}^M \frac{\tilde{\alpha}_{11}^{(m)} / \tau_\alpha^{(m)}}{p + (\tau_\alpha^{(m)})^{-1}} \mathbf{\Theta}_\star + \sum_{o=1}^O \frac{\tilde{\alpha}_{33}^{(o)} / \tau_\alpha^{(o)}}{p + (\tau_\alpha^{(o)})^{-1}} \mathbf{N}_\star \right) \tilde{\theta}^*(p) \\ &= \tilde{\beta}_g^*(p) + \sum_{m=1}^M \frac{\tilde{\alpha}_{11}^{(m)} \tilde{\theta}^*(p)}{\tau_\alpha^{(m)} (p + (\tau_\alpha^{(m)})^{-1})} \mathbf{\Theta}_\star + \sum_{o=1}^O \frac{\tilde{\alpha}_{33}^{(o)} \tilde{\theta}^*(p)}{\tau_\alpha^{(o)} (p + (\tau_\alpha^{(o)})^{-1})} \mathbf{N}_\star,\end{aligned}\quad (26)$$

where  $\tilde{\sigma}_g^*(p)$  and  $\tilde{\beta}_g^*(p)$  are the Laplace-Carson transform of the glassy responses in terms of stress and thermal strains, respectively. Introducing three sets of second order tensor internal variables  $\{\mathbf{q}_L^{*(n_b)}\}$ ,  $\{\mathbf{q}_{\alpha_1}^{*(m)}\}$  and  $\{\mathbf{q}_{\alpha_3}^{*(o)}\}$  the foregoing equations reads:

$$\begin{aligned}\tilde{\sigma}^*(p) &= \tilde{\sigma}_g^*(p) - \sum_{b=1}^6 \sum_{n_b=1}^{N_b} \tilde{l}^{(n_b)} \mathbf{H}_\star^{(b)} : \mathbf{q}_L^{*(n_b)}(p), & \mathbf{q}_L^{*(n_b)}(p) &= \frac{\tilde{\epsilon}^*(p) - \tilde{\beta}^*(p)}{\tau_L^{(n_b)} (p + (\tau_L^{(n_b)})^{-1})} \\ \tilde{\beta}^*(p) &= \tilde{\beta}_g^*(p) + \sum_{m=1}^M \mathbf{q}_{\alpha_1}^{*(m)}(p) + \sum_{o=1}^O \mathbf{q}_{\alpha_3}^{*(o)}(p), & \mathbf{q}_{\alpha_1}^{*(m)}(p) &= \frac{\tilde{\alpha}_{11}^{(m)} \tilde{\theta}^*(p) \mathbf{\Theta}_\star}{\tau_\alpha^{(m)} (p + (\tau_\alpha^{(m)})^{-1})}, & \mathbf{q}_{\alpha_3}^{*(o)}(p) &= \frac{\tilde{\alpha}_{33}^{(o)} \tilde{\theta}^*(p) \mathbf{N}_\star}{\tau_\alpha^{(o)} (p + (\tau_\alpha^{(o)})^{-1})}\end{aligned}$$

(27)

Reordering the expressions of the internal variables and performing the inverse transform of the equations in Eq. (27) we obtain equivalent forms to those presented in [52]. the internal-time forms and the associated O.D.E's of the internal variables are obtained as follows:

$$\begin{aligned}\bar{\sigma}(\xi) &= \bar{\sigma}_g(\xi) - \sum_{b=1}^6 \sum_{n_b=1}^{N_b} \tilde{l}^{(n_b)} \mathcal{H}_\star^{(b)} : \mathbf{q}_L^{(b,n_b)}(\xi), & \frac{d}{d\xi} \mathbf{q}_L^{(n_b)}(\xi) + \frac{1}{\tau_L^{(n_b)}} \mathbf{q}_L^{(n_b)}(\xi) &= \frac{\bar{\epsilon}(\xi) - \tilde{\beta}(\xi)}{\tau_L^{(n_b)}}, \\ \tilde{\beta}(\xi) &= \tilde{\beta}_g(\xi) + \sum_{m=1}^M \mathbf{q}_{\alpha_1}^{(m)}(\xi) + \sum_{o=1}^O \mathbf{q}_{\alpha_3}^{(o)}(\xi), & \frac{d}{d\xi} \mathbf{q}_{\alpha_1}^{(m)}(\xi) + \frac{1}{\tau_{\alpha}^{(m)}} \mathbf{q}_{\alpha_1}^{(m)}(\xi) &= \frac{\tilde{\alpha}_{11}^{(m)} \tilde{\theta}(\xi) \Theta_\star}{\tau_{\alpha}^{(m)}}, & \frac{d}{d\xi} \mathbf{q}_{\alpha_3}^{(o)} + \frac{1}{\tau_{\alpha}^{(o)}} \mathbf{q}_{\alpha_3}^{(o)} &= \frac{\tilde{\alpha}_{33}^{(o)} \tilde{\theta}(\xi) \mathcal{N}_\star}{\tau_{\alpha}^{(o)}}.\end{aligned}\quad (28)$$

The computed stress is then obtained in the internal-time domain. Thanks to the mapping  $t \mapsto \xi$ , quantities measured in the internal time take the same values in the correspondent observer times, in fact since the values of  $\xi$  are computed as an initial step for a given temperature at a given instant, the return to the observer time is trivial. For the simulation examples, the non-homogeneous ODE's characterizing the evolution of the internal variables are solved numerically by implementing the Taylor's integration scheme [59]. This methodology is based on the assumption of a linear evolution of the right-hand side of the ODE's for the computation of its particular solution. The discrete evolution equation for an ODE relating second order tensorial functions (Eq. (28)), for instance, an arbitrary internal variable  $\mathbf{q}(\xi)$ , and a right-hand side  $\frac{\Upsilon(\xi)}{\tau}$ , is written down as follows:

$$\begin{aligned}\forall \xi_k &\in \{0, \xi_2, \dots, \xi_k, \dots, \xi_K\}, \quad \text{and}, \quad \Delta \xi_{k+1} = \xi_{k+1} - \xi_k \\ \mathbf{q}(\xi_{k+1}) &= \mathbf{q}(\xi_k) e^{-\frac{\Delta \xi_{k+1}}{\tau}} + \Upsilon(\xi_k) \left(1 - e^{-\frac{\Delta \xi_{k+1}}{\tau}}\right) + (\Upsilon(\xi_{k+1}) - \Upsilon(\xi_k)) \left(1 - \frac{\tau}{\Delta \xi_{k+1}} (1 - e^{-\frac{\Delta \xi_{k+1}}{\tau}})\right)\end{aligned}\quad (29)$$

## 4.2. Problems setting

### Macroscopic loading:

Three scenarios of simulation are presented. All these situations consider a linear cooling while different mechanical constraints are applied to the REV. Five constant cooling rate ( $\dot{\theta}$ ) are studied, from very fast (8.64s) to slow cooling (24h). The cooling rate iterations are given by  $\Delta \bar{T}/t_c$ , with  $t_c$  being the cooling times, previously presented in Fig. 5, and  $\Delta T$  the total variation of temperature, here,  $-225^\circ\text{C}$ . Numerical values are presented below.

$$\dot{\theta} \in \{-0.00260417, -0.0260417, -0.260417, -2.60417, -26.0417\} [^\circ\text{C s}^{-1}].$$

For the mechanical constraints, three different cases are considered: the strains-free case, this is,  $\bar{\epsilon}(t) = \mathbf{0}$  (**load case 1**). The second case is the stress-free case, this is,  $\bar{\sigma}(t) = \mathbf{0}$  (**load case 2**). Finally, the mixed conditions' case is implemented, this is,  $\bar{\sigma}_{22}(t) = 0$  and  $\bar{\epsilon}_{33}(t) = \bar{\epsilon}_{11}(t) = 0$  (**load case 3**), which corresponds to the case of a laminate composed by two thin plates with an angle of relative deviation of the material's symmetry axis of  $90^\circ$  with  $\mathbf{e}_2$  being the stacking direction of the laminate.



**Sensibility to the starting temperature:**

The study range of the temperature characterizing the FDM 3D-printing of a PEI filaments is between 355°C to room temperature ( $\approx 25^\circ\text{C}$ ). Primary studies of the amorphous PEI-like matrix used in the present work have suggested the quasi-pure dissipative behavior between 355 and 250°C, reflected by a negligible amount of residual stress produced within this temperature interval. This can be identified easily by observing the values of  $a_T(T)$  associated to high temperatures, it is observed that, the amount of viscous strain is increased at high temperatures as most of the relaxation mechanisms are activated simultaneously. The influence of the starting temperature on the magnitude of the residual stress is presented in Fig. 8. This analysis was performed at maximum cooling rate as it is the one giving the highest levels of stress. From this figure, it is clear that the generation of stress at high temperature is negligible compared to the level produced as the glass transition temperature ( $T_g = 216^\circ\text{C}$ ) is closer and below it. The maximum relative error on the stress is close to 2%. For the interest of the present work, low stages of stress are not displayed. In conclusion, the starting temperature is set to  $T(0) = 250^\circ\text{C}$ , which imposes the before mentioned  $\Delta T = -225^\circ\text{C}$ .

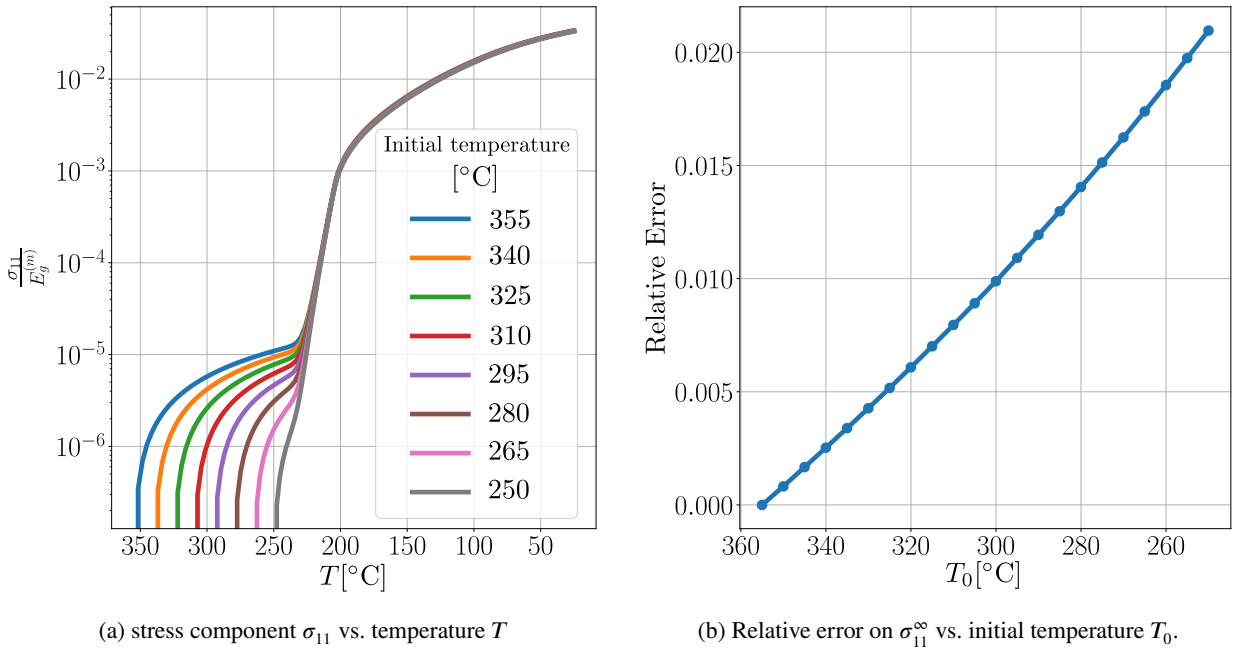


**Figure 8:** Influence of the starting temperature  $T_0$  of the simulation on the magnitude of the residual stress at minimum cooling time (8.64[s]). Study performed for the load case 1 (Section 4.4).

### 4.3. Numerical considerations

Reference solutions are obtained from FFT-based full-field homogenization [45] by using the in-house code Craft<sup>1</sup>. This method uses 3D images discretized in voxels for the REVs (Fig. 9). The fibers' are represented by long capsules (cylinders with hemispherical ends), that is closer to the actual geometry of the fibers. In contrast, mean-field schemes uses prolate spheroids as representation for the fibers. For this study, it is considered a spheroid that preserves the quadratic moment of the capsule used in the full-field simulations instead of keeping the same aspect ratio [19], this is,  $w_0 = w_0^{\text{ref}}(2/\sqrt{3})$ . Comparison data of the consequences of the precedent choice is presented in Fig. 10. In this figure, the error is measured just on the Lielens scheme, comparing the closeness of the asymptotic stress with the reference solutions. Finally, the simulations used for these plots consider the case of maximum volume fraction ( $c^{(f)} = 40\%$ ) as it represents a greater influence of the presence of fibers on the macroscopic behavior.

The computational 3D REVs for the simulations are generated using the probability distribution functions described in Section 3. The generation task has to ensure the non superposition of fibers as priority, in consequence the distributions are exposed to violations during the sampling process, this is why after generation, the distribution

<sup>1</sup><http://craft.lma.cnrs-mrs.fr/>

parameters are refitted from the generated microstructures to avoid the loss of accuracy when comparing the mean-field data (in results, only theoretical values of the distribution parameters are displayed).

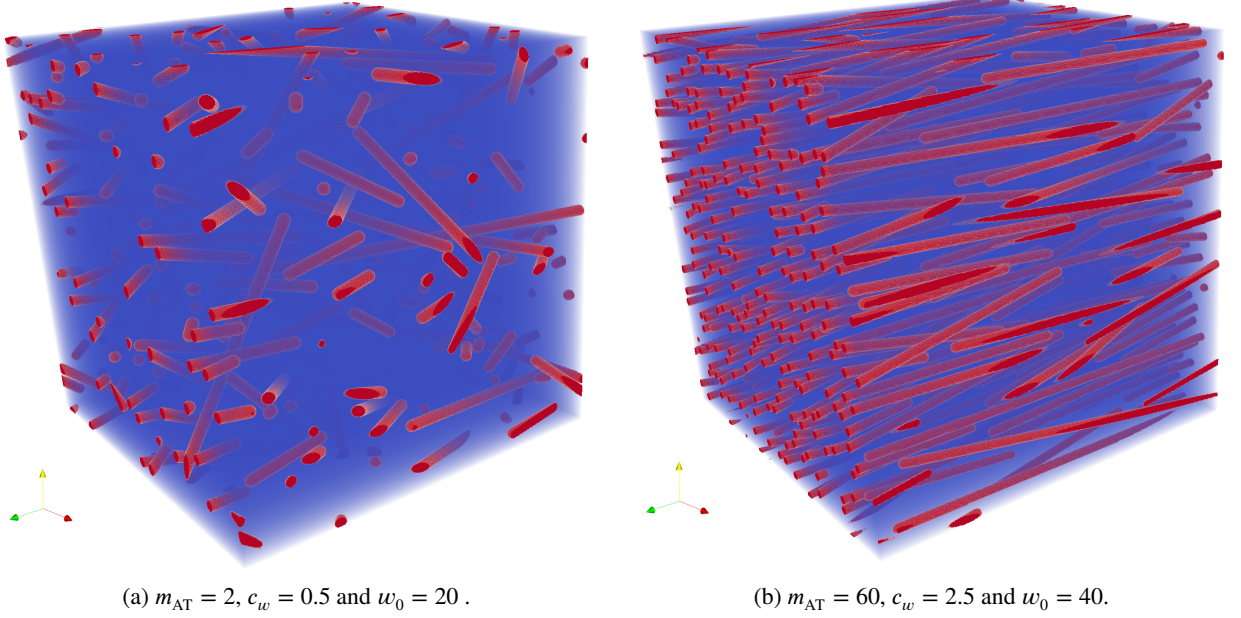


**Figure 9:** Examples of computer generated representative elementary volumes (REV) used in the computation of reference solutions. The volume fraction of fibers in the displayed microstructures is  $c^{(f)} = 10\%$ . On the left side, the more disoriented case with a higher variability of lengths. On the right side, the most oriented and less variable lengths.

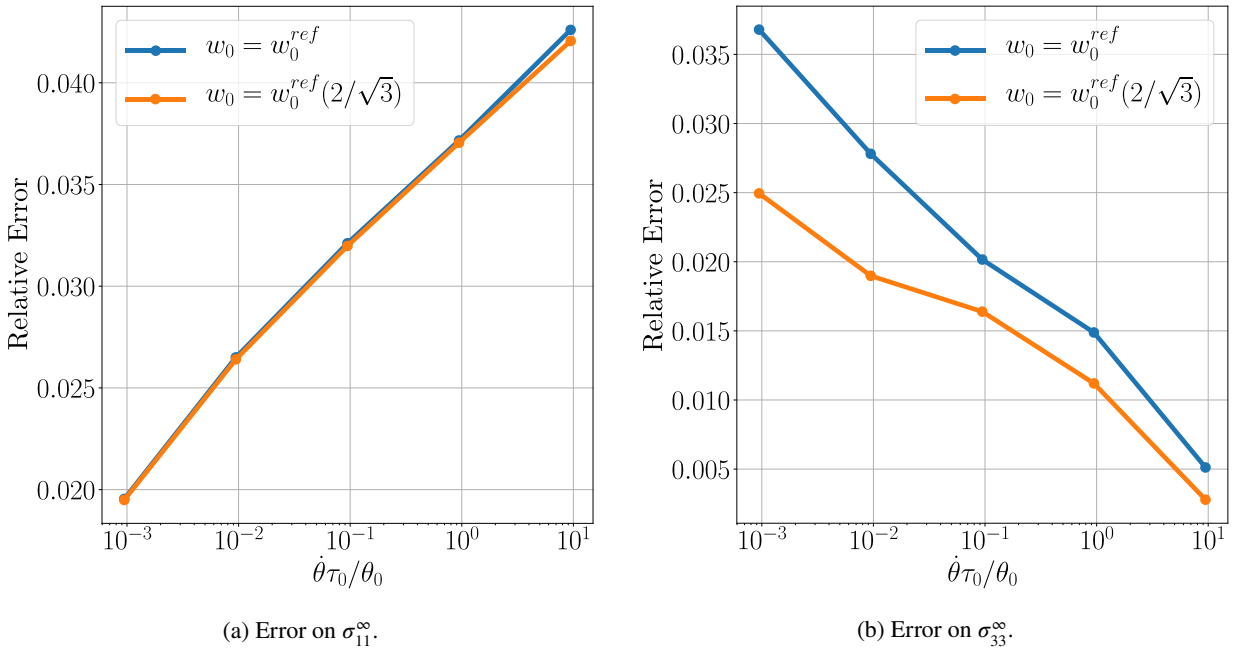


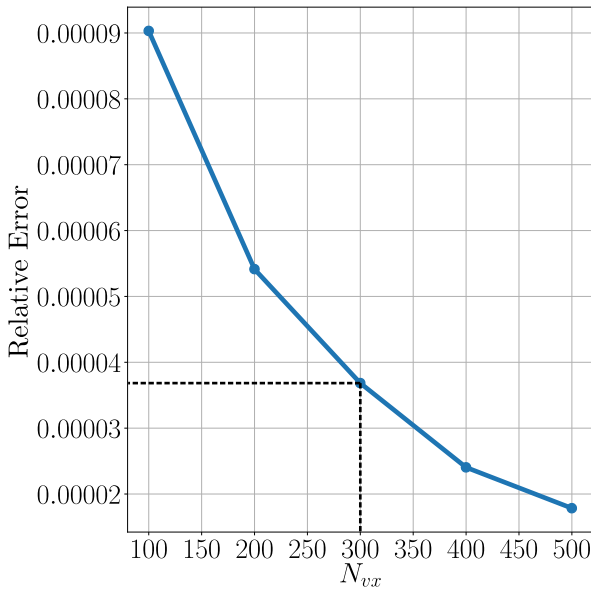
**Figure 10:** Relative error of the inclusions' representation, measured on the asymptotic stress for Lielens' scheme vs. normalized cooling rate. volume fraction  $c^{(f)} = 40\%$ . Distribution parameters,  $m_{AT} = 60$ ,  $c_w = 2.5$  and  $w_0 = 40$ .

**Discretization and Sampling convergence:** Due to the high cost in terms of computation time of reference solutions, the discretization of the REV is limited by the computation capabilities of the available hardware. This is why a study of discretization convergence is performed to improve the time of computations. By imposing a maximum admissible error of  $1.0 \times 10^{-4}$ , the microstructure discretization is set to  $300 \times 300 \times 300$  voxels. On the other hand, a study characterizing the convergence in terms of the number of inclusions is performed too. This is equivalent to the study of the size of the REV, as the dimensions of the fibers are obtained by relative sizing from the total volume and the volume fraction; this study characterizes the accuracy of the representation of the REV with respect to the whole composite volume. Similarly, by imposing the maximum error in the number of fibers to  $1.5 \times 10^{-4}$ , the number of inclusions for the simulations is set to 300 fibers. Results of the Convergence studies are presented in Fig. 11. In addition, in Table. 2 the times for reference and mean-field solutions' computations are presented, the values correspond to the "faster" FFT simulation and its correspondent obtained through mean-field schemes. In the case of the reference solutions, each simulation was obtained in two computational nodes with 56 cores and 128 Gigabytes of RAM.

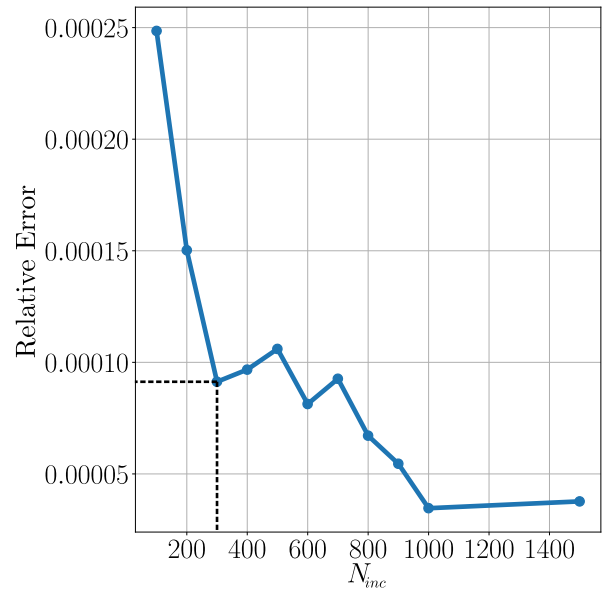
For mean-field computations, a machine with 16 cores and 128 Gigabytes of RAM was used. As can be noted from the table, even under less computational power conditions, the time for mean-field computations is always negligible compared to the full-field reference solutions. In fact, as the effective behavior is in an explicit form, the computation of effective behavior (in the Laplace-Carson domain) is a fraction of the time shown in the table. Most of the time is consumed in approximating effective Prony-series and computing each simulation scenario.

**Table 2**  
Time of computations for effective residual stress simulations

Method	Time (h.m.s.)
FFT(300x300x300)	05:11:17
FFT(400x400x400)	08:04:21
FFT(500x500x500)	12:19:03
Mean-field	00:02:46



(a) Error on  $\bar{\sigma}^\infty$  vs number of voxels per edge ( $N_{vx}$ ).



(b) Error on  $\bar{\sigma}^\infty$  vs number of inclusions ( $N_{inc}$ ).

**Figure 11:** Convergence study for reference solutions. volume fraction  $c^{(f)} = 40\%$ . Distribution parameters,  $m_{AT} = 60$ ,  $c_w = 2.5$  and  $w_0 = 40$ .

#### 4.4. Comparisons

Here, results are presented for the simulations settings specified in Section 4.2. The solutions are obtained for multiple combination of microstructural parameters, that are, the volume fraction  $c^{(f)}$ , the orientation distribution parameter  $m_{AT}$ , and length distribution parameters  $w_0$  and  $c_w$ . Numerical values of the parameters are presented in the Table. 3. All combinations of parameters have been tested, and as can be noted this represents a large amount of data. For the sake of clarity in comparisons, just some representative combinations are presented for each load case.

Simulation results are presented as follows: First, for each load case, the evolution of the computed mechanical quantities is presented in function of the temperature (figures Fig. 12, Fig. 17 and Fig. 22). Each of these figures shows the evolution for three different values of the imposed cooling rate, from the slowest (blue lines) passing by a middle velocity (green lines), to the fastest (purple lines). As can be noted from the gaps in each group, they are almost consistent in each figure, this fact verifies the ability of the method to predict residual stress in a wide range of cooling rates. Then, having this initial figures for each load case, the influence of the microstructural parameters is studied by presenting the asymptotic value of the mechanical quantities as a function of the microstructural parameters by sweeping in one parameter while the rest of them remains constant and equal to the values of the evolution plots: Figures Fig. 13, Fig. 18 and Fig. 23 showing the influence of the volume fraction  $c^{(f)}$ , figures Fig. 14, Fig. 19 and Fig. 24 presents the influence of the Advani-Tucker orientation parameter  $m_{AT}$ . To study the influence of the length distribution parameters (Weibull's law), Figures Fig. 15, Fig. 20 and Fig. 25 show the influence of  $c_w$ , and figures Fig. 16, Fig. 21 and Fig. 26 present the influence of  $w_0$ . Regarding the plotted stress, it is normalized by the elastic response of the matrix  $\sigma^{(m),e}$ .

From all these figures, the high accuracy of the proposed methodology is verified noting that, Lielens' scheme is almost always slightly closer to the reference solutions, but despite this fact the magnitude of the gaps are negligible between the implemented mean-field schemes. The closeness of the responses of the Mori-Tanaka and IDD schemes is explained from the fact that the IDD approximation was computed using a unique spatial distribution cell which aspect ratio is very close to the fiber's mean aspect ratio ( $w^{(D,r)} = 0.8w_0$ ). A better use of the capabilities of this scheme should consider a non-uniformly distributed spatial distribution cell ( $\Omega^{(D,r)}$ ) space using a probabilistic distribution, as it was for example implemented for the variation in the fiber lengths and suggested in [63]. As inferred in [39], the Lielens' scheme is able to improve the approximation of the effective behavior at higher volume fractions of the fibrous phase by considering the computation of localization tensors as an interpolation of the Mori-Tanaka scheme and another one obtained by considering the same estimate but in a case in which the fibers become the continuous phase and the matrix the dispersed one. The latter justifying why this approximation shows better results when comparing the asymptotic responses as a function of the volume fraction (Fig. 13, Fig. 18 and Fig. 23), anyway considering the volume fraction interval in the present work, that is representative of the charge of fibers in composite filaments for HT-FRAM technology, the gaps between the mean-field schemes are not so significant which explains the closeness between all of them. In the same fashion, the effects of the variations of the microstructural parameters (i.e. length and orientation distributions) representing the particular state of the fibers inside the composite filament are enhanced by Lielens approach. Regarding the effect of the variation of the orientation parameter  $m_{AT}$ , in Fig. 14, Fig. 19 and Fig. 24, the mean-field approach exhibits consistency in all cases when going from the more disoriented distribution (more isotropic) to the more filament axis aligned distribution (increasing the stiffness in the axis direction). However, the proposed methodology and the reference solutions are slightly closer in the cases where the fiber orientation disorder increases (lower values of the Advani and Tucker parameter). Finally, considering the variation of the length parameters  $w_0$  and  $c_w$ , representing the mean length and intensification of the distribution around this value respectively. The simulation results are still consistent when considering combinations resulting in microstructures of long fibers and more or less homogeneous in distribution, with those that have a distribution of different lengths. The variations of the gaps are always on the same order, and as pointed out before Lielens' scheme is always better at accounting the effect of these variations when comparing with reference solutions. From the aforementioned, one can conclude that any of these three methods could be a good choice, however it must be noted that if one aims to make an objective choice based on the quality and the complexity of the implementation, the choice should be the Mori-Tanaka Scheme.

##### Load case 1:

Due to the fact that the imposed macroscopic strain is  $\bar{\epsilon}(t) = \mathbf{0}$ , this case presents the highest levels of stress. The figure Fig. 13 showing the normalized asymptotic stress in function of the volume fraction allows seeing the effect of the reinforcement in the macroscopic behavior, then from the left to the right side the values of the normalized stress are always increasing as the effective relaxation moduli tensor increases in magnitude. The figure Fig. 14, showing

**Table 3**  
Microstructural parameters for simulations

Parameter	Values				
$m_{AT}$	2	10	60	-	-
$c_w$	0.5	1.5	2.5	-	-
$w_0$	20	30	40	-	-
$c^{(f)}$	0.1	0.2	0.3	-	0.4

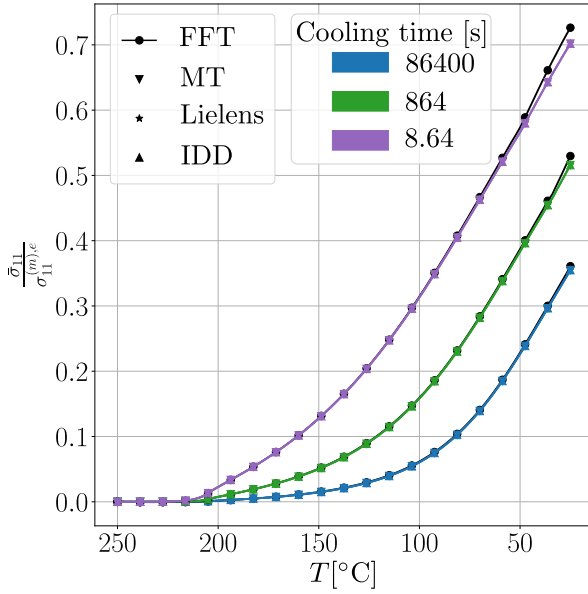
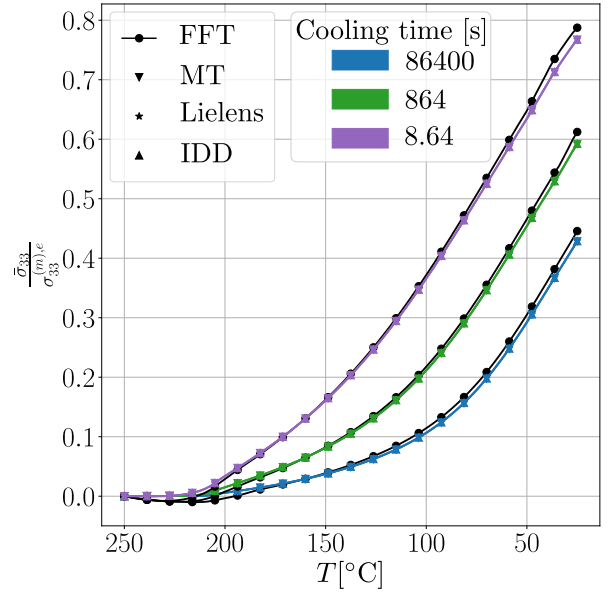
the normalized asymptotic stress on-plane and on-axis, allows seeing the level of anisotropy in terms of the principal directions  $e_1$  and  $e_3$ . from the less to the most oriented, one can see how the level of isotropy decrease as the fibers become more organized around the filament axis, the ability of the probabilistic approach to map these variations is then verified because the gap between reference and mean-field solutions is almost consistent. From these figures, one can note that it is difficult to differentiate the gap between the different mean-field schemes implemented in the comparisons. Indeed, it seems that the three of them are giving high quality approximations. To be able to compare between them. The figure Fig. 15 and Fig. 16 showing the influence of the length distribution parameters shows small variations of the observed stress as these parameters varies; regarding Fig. 15 and considering that the fixed value of  $m_{AT}$  is 10 which represents a larger number of fibers in the filament axis direction (Fig. 7), one can note how the fact of increasing the number of fibers with a length that is close to the mean value  $w_0 = 30$ , significantly increases the asymptotic response of the stress in the filament axis direction compared to the behavior in the transverse plane. Looking at the variations of the asymptotic stress as a function of the mean length  $w_0$ , and holding the distribution parameter  $c_w$  to 1.5, a decrease in the asymptotic stress is observed as  $w_0$  increases, this can be interpreted supported by Fig. 6 in which this fact gives as output a "more distributed" population of fibers but always being notably higher to the side of the shorter fibers, then as the diameter of fibers is considered constant the fact that shorter fibers are populating the REV gives an effective stiffness that is lower, ergo it is reasonable that the asymptotic stress decrease. From all the figures showing the asymptotic response, it is confirmed that despite the scheme chosen for the approximations, all of them are very close to the reference solutions. Anyway, Lielens scheme is always slightly better in all situations.

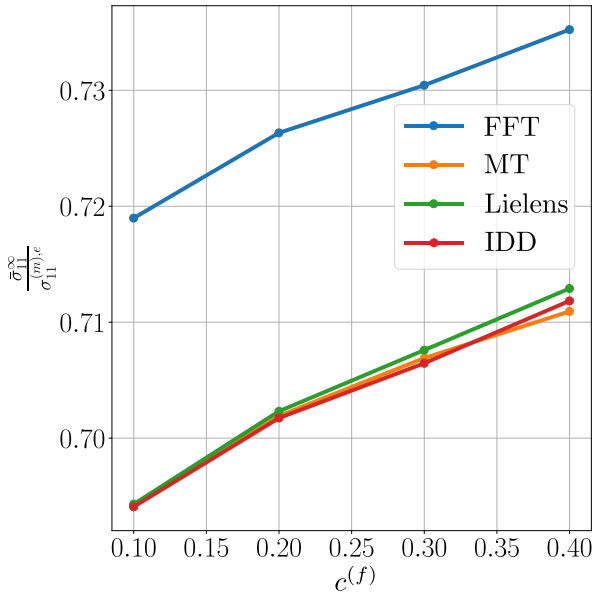
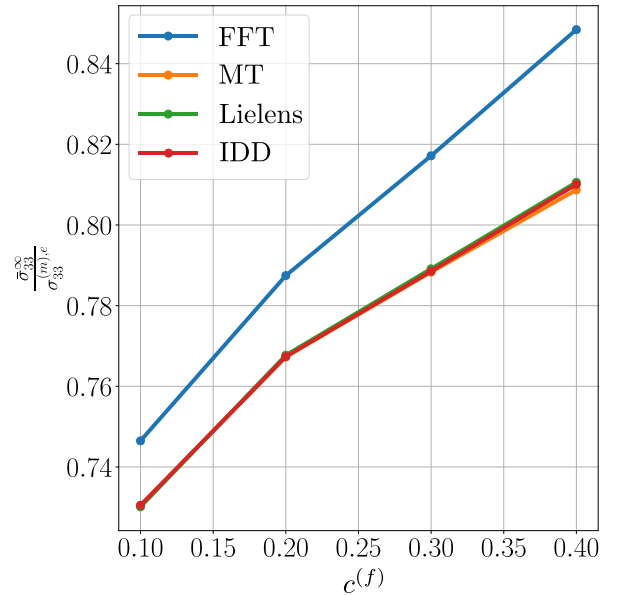
### Load case 2:

In this case, the macroscopic stress  $\bar{\sigma}$  is set to  $\mathbf{0}$  in the REV, therefore the corresponding strain solution is equal to the macroscopic thermal strain, since it is the only source of deformation in the REV. As can be noted from the figures of this case (Figs. 17-21), the computed macroscopic strains remain inside the linear domain, which validates the material model adopted in the present work, that is linear viscoelastic. The figure Fig. 17 showing the evolution of the strain elements in function of temperature confirms the consistency of the methodology when computing stress or strain. Similarly to the load case 1, in figure Fig. 19 the degree of anisotropy is controlled via the values of  $m_{AT}$ , the effect of the reinforcement in the macroscopic strain presented in Fig. 18 shows the high accuracy of the proposed procedure as the solutions are very close to the reference (FFT), specially when regarding the filament axis direction ( $e_3$ ). When looking figures Fig. 20 and Fig. 21 one can note how the macroscopic strain decreases as the parameters increases, this represents the fact that the mean length of the fibers increases and the number of fibers associated to this value increases.

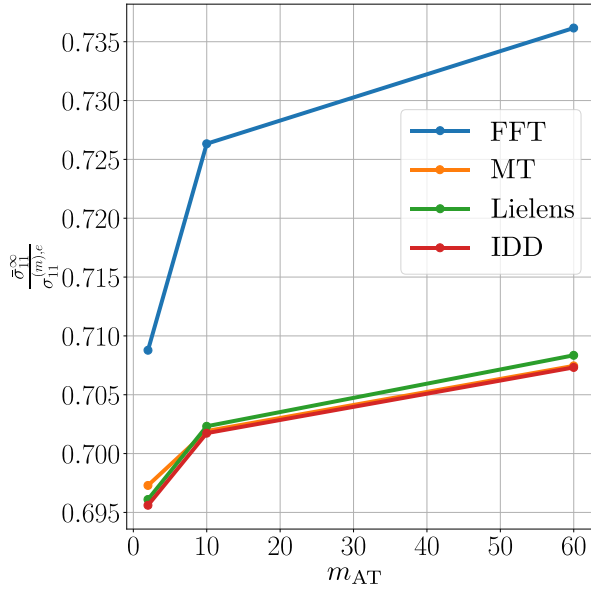
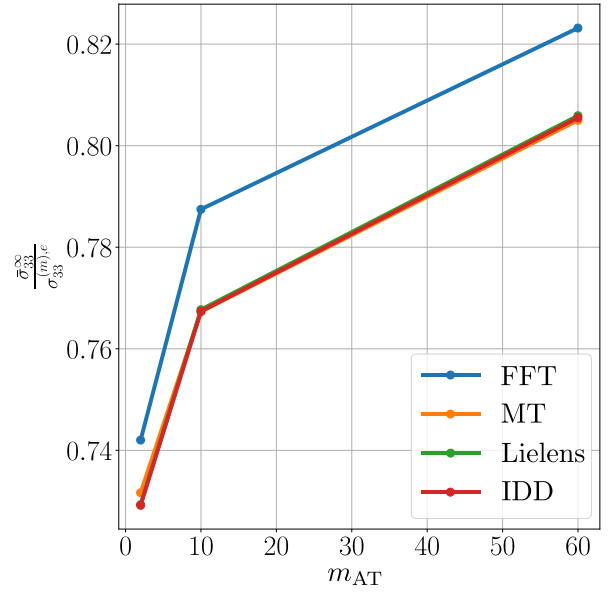
### Load case 3:

This is the case of mixed macroscopic constraints, here the laminate case, in which the stacking direction is  $e_2$ . Results are presented in the same way as the precedent load cases, Fig. 22 shows the evolution of the showing the non-zero elements of the mechanical response ( $\bar{\epsilon}_{22} = \bar{\epsilon}_{11}$  and  $\bar{\sigma}_{33}$ ) in function of temperature. In agreement with the precedent cases, the solutions plotted show remarkable accuracy compared to reference solutions in both, stress and strain. Similarly to the precedent load cases, the influence of the microstructural parameters in presented in figures Fig. 23- 26. In the same way as for the precedent load cases, Lielens schemes seems to be slightly better when estimating both, macroscopic stress or strain.

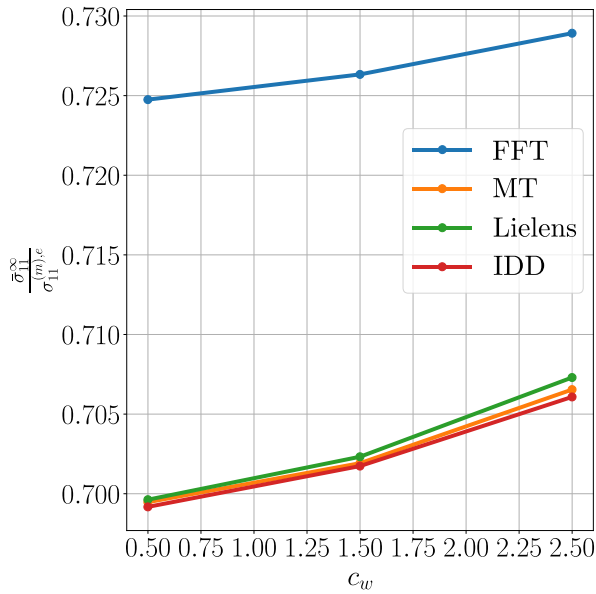
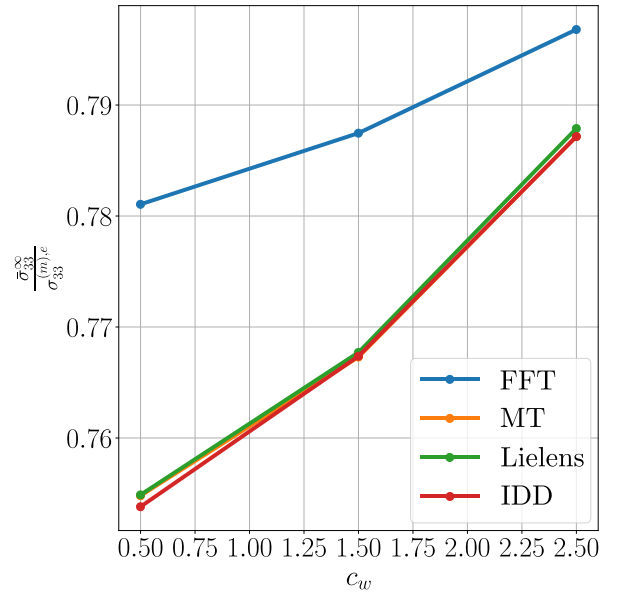

 (a) On-plane residual stress ( $\sigma_{11}$ ).

 (b) Filament axis residual stress ( $\sigma_{33}$ ).

**Figure 12:** Normalized stress vs. temperature ( $T$ ), computed for load case 1,  $c^{(f)} = 0.2$ ,  $m_{\text{AT}} = 10$ ,  $c_w = 1.5$  and  $w_0 = 30$ .

 (a) On-plane residual stress ( $\sigma_{11}$ ).

 (b) Filament axis residual stress ( $\sigma_{33}$ ).

**Figure 13:** Asymptotic normalized stress vs. the volume fraction ( $c^{(f)}$ ), computed for load case 1, Cooling time = 8.64[s],  $m_{\text{AT}} = 10$ ,  $c_w = 1.5$  and  $w_0 = 30$ .

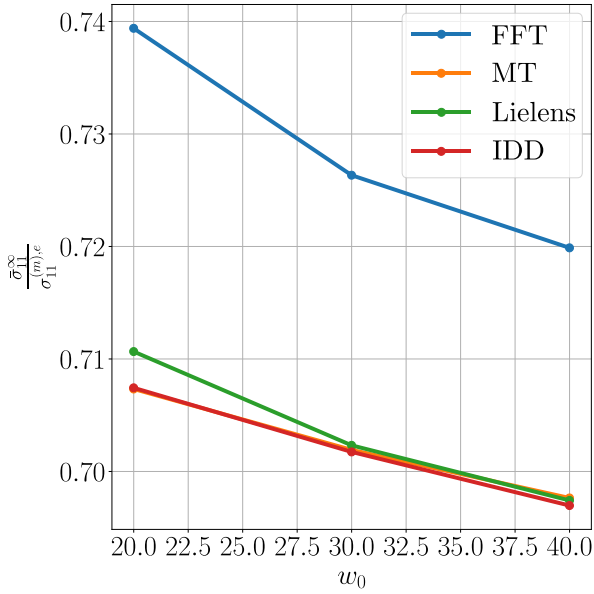
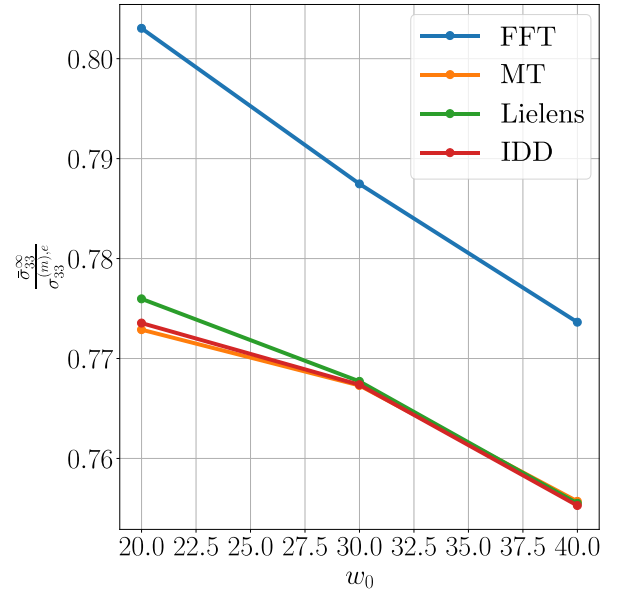

 (a) On-plane residual stress ( $\sigma_{11}$ ).

 (b) Filament axis residual stress ( $\sigma_{33}$ ).

**Figure 14:** Asymptotic normalized stress vs. the Advani-Tucker parameter  $m_{AT}$ , computed for load case 1, Cooling time = 8.64[s],  $c^{(f)} = 0.2$ ,  $c_w = 1.5$  and  $w_0 = 30$ .

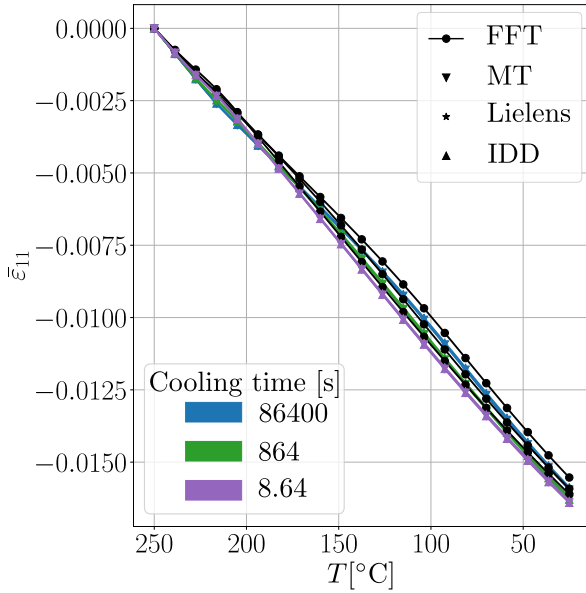
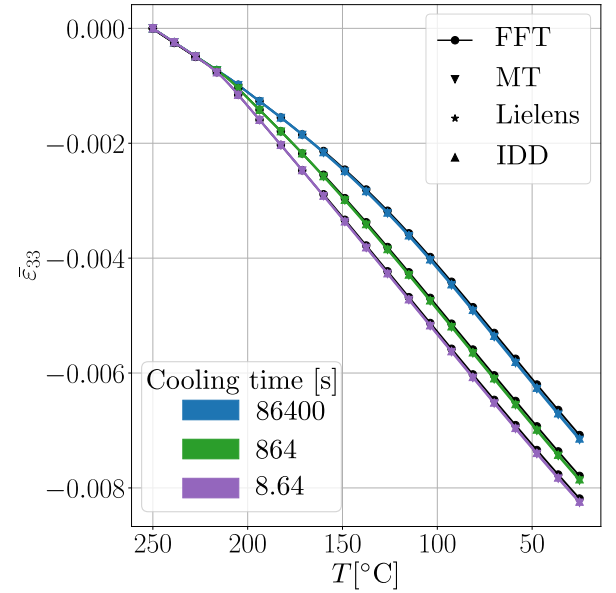

 (a) On-plane residual stress ( $\sigma_{11}$ ).

 (b) Filament axis residual stress ( $\sigma_{33}$ ).

**Figure 15:** Asymptotic normalized stress vs. the Weibull's parameter  $c_w$ , computed for load case 1, Cooling time = 8.64[s],  $c^{(f)} = 0.2$ ,  $m_{AT} = 10$  and  $w_0 = 30$ .

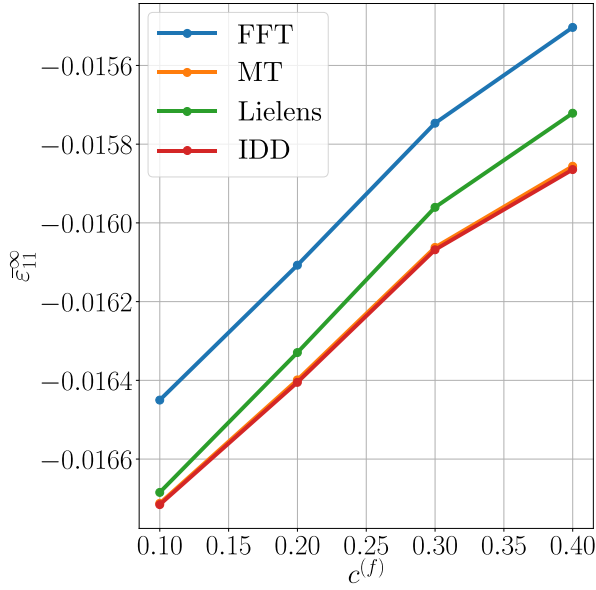
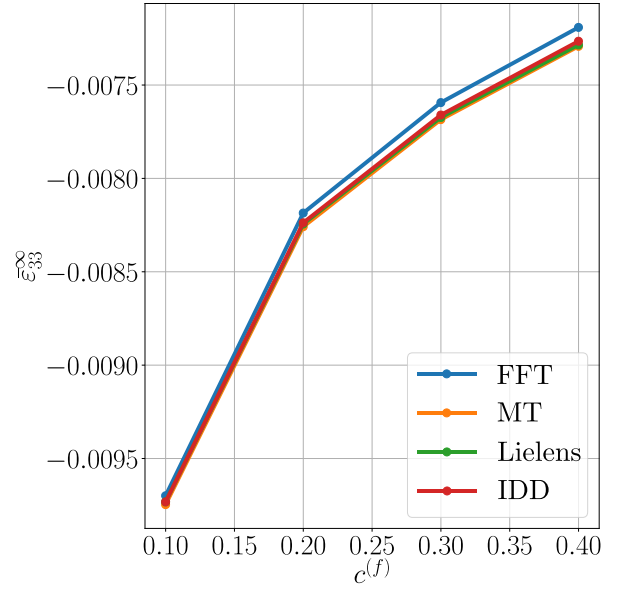



 (a) On-plane residual stress ( $\sigma_{11}$ ).

 (b) Filament axis residual stress ( $\sigma_{33}$ ).

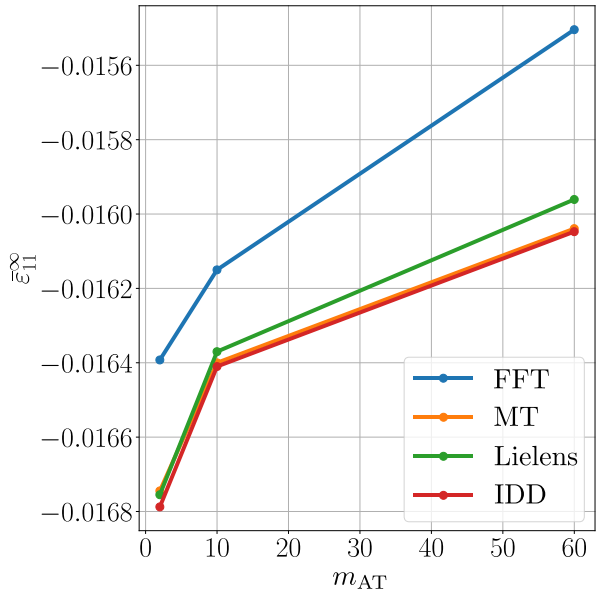
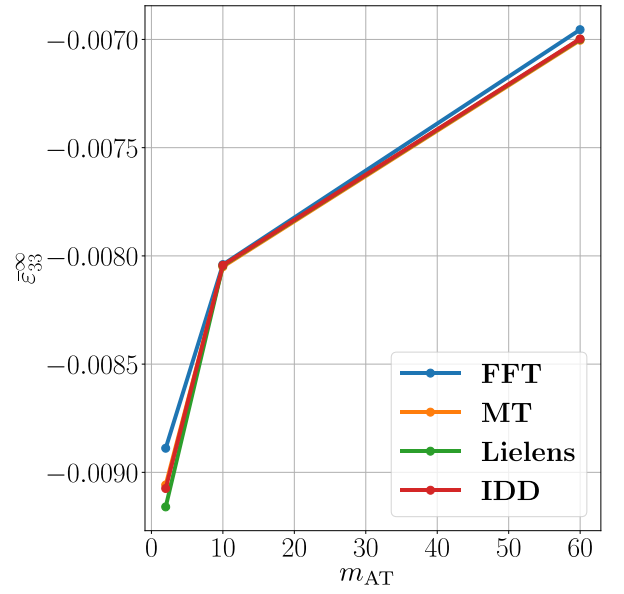
**Figure 16:** Asymptotic normalized stress vs. the Weibull's parameter  $w_0$ , computed for load case 1, Cooling time = 8.64[s],  $c^{(f)} = 0.2$ ,  $m_{AT} = 10$  and  $c_w = 1.5$ .


 (a) On-plane residual strain ( $\varepsilon_{11}$ ).

 (b) Filament axis residual strain ( $\varepsilon_{33}$ ).

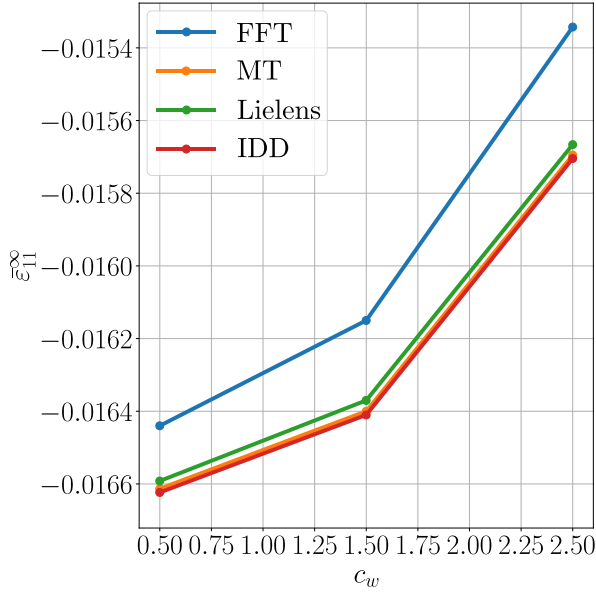
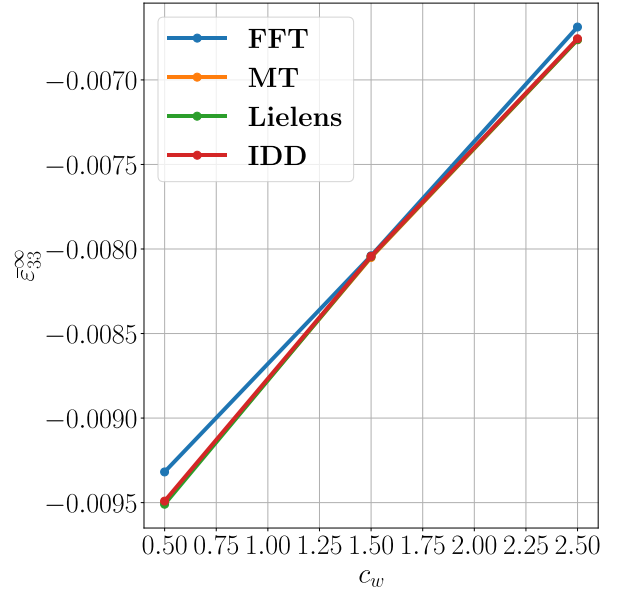
**Figure 17:** Strain vs. temperature ( $T$ ), computed for load case 2,  $c^{(f)} = 0.2$ ,  $m_{AT} = 10$ ,  $c_w = 1.5$  and  $w_0 = 30$ .


 (a) On-plane residual strain ( $\epsilon_{11}$ ).

 (b) Filament axis residual strain ( $\epsilon_{33}$ ).

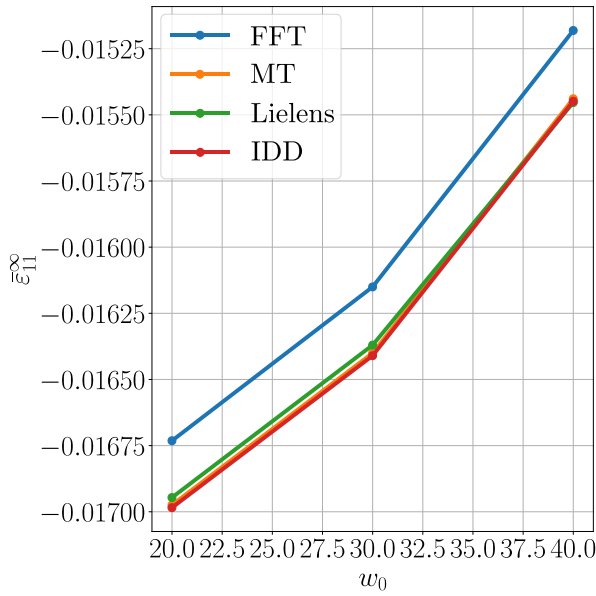
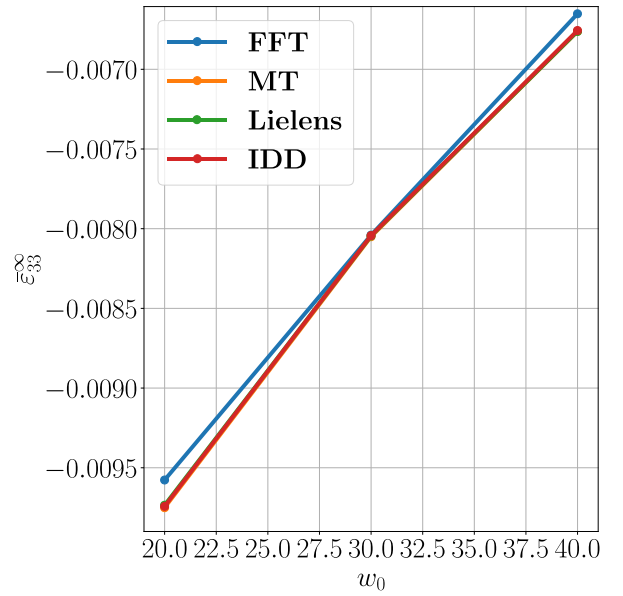
**Figure 18:** Asymptotic strain vs. the volume fraction ( $c^{(f)}$ ), computed for load case 2, Cooling time = 8.64[s],  $m_{AT} = 10$ ,  $c_w = 1.5$  and  $w_0 = 30$ .


 (a) On-plane residual strain ( $\epsilon_{11}$ ).

 (b) Filament axis residual strain ( $\epsilon_{33}$ ).

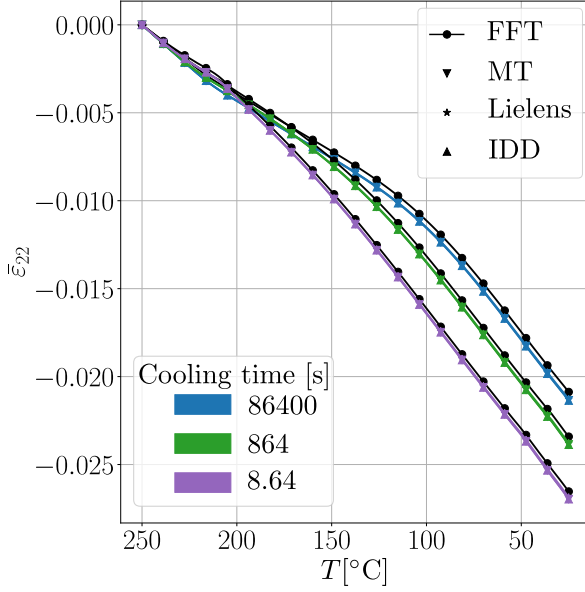
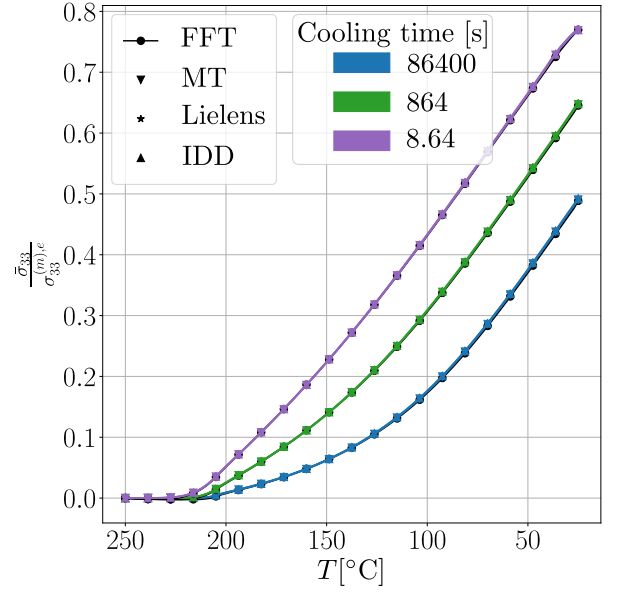
**Figure 19:** Asymptotic strain vs. the Advani-Tucker parameter ( $m_{AT}$ ), computed for load case 2, Cooling time = 8.64[s],  $c^{(f)} = 0.2$ ,  $c_w = 1.5$  and  $w_0 = 30$ .


 (a) On-plane residual strain ( $\epsilon_{11}$ ).

 (b) Filament axis residual strain ( $\epsilon_{33}$ ).

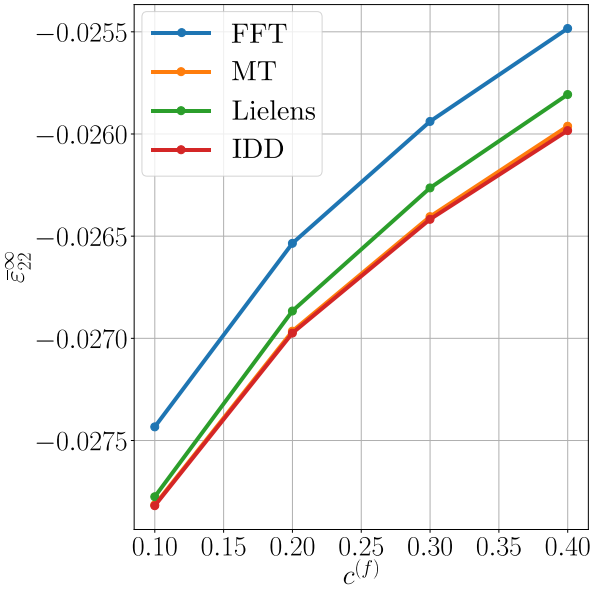
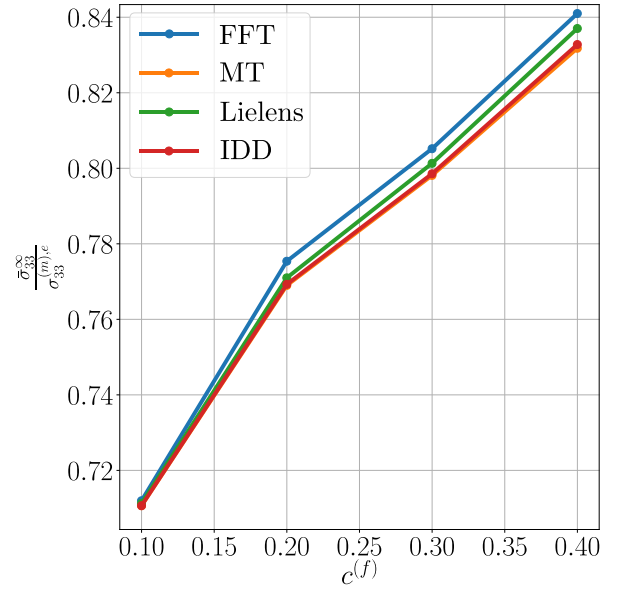
**Figure 20:** Asymptotic strain vs. the Weibull parameter  $c_w$ , computed for load case 2, Cooling time = 8.64[s],  $c^{(f)} = 0.2$ ,  $m_{AT} = 10$  and  $w_0 = 30$ .


 (a) On-plane residual strain ( $\epsilon_{11}$ ).

 (b) Filament axis residual strain ( $\epsilon_{33}$ ).

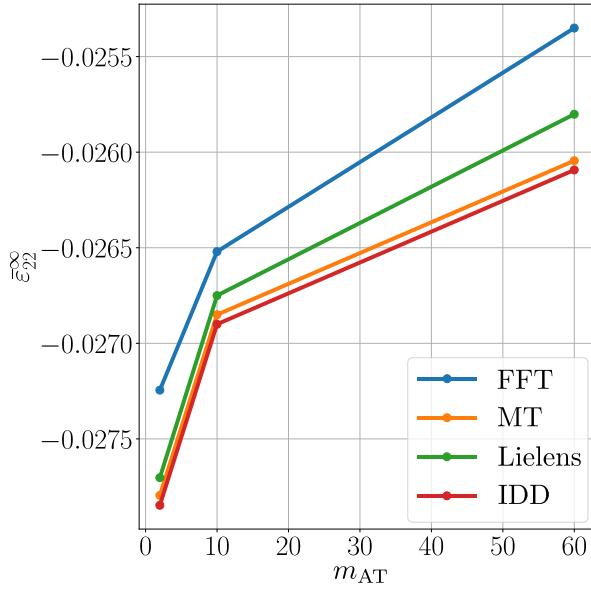
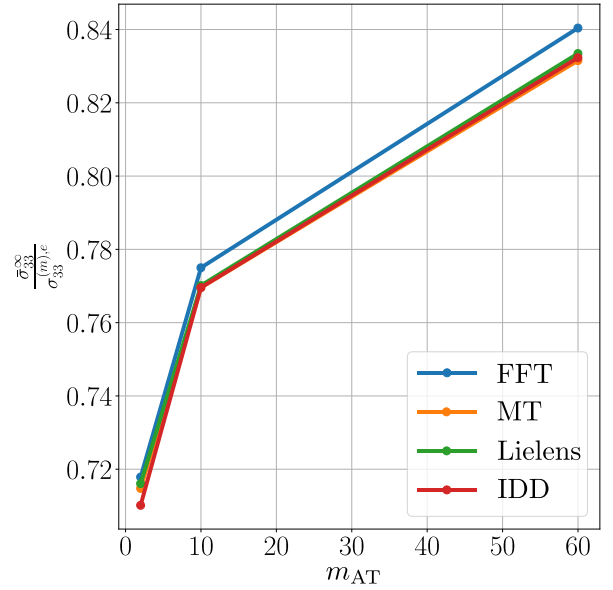
**Figure 21:** Asymptotic strain vs. the Weibull parameter  $w_0$ , computed for load case 2, Cooling time = 8.64[s],  $c^{(f)} = 0.2$ ,  $m_{AT} = 10$  and  $c_w = 1.5$ .

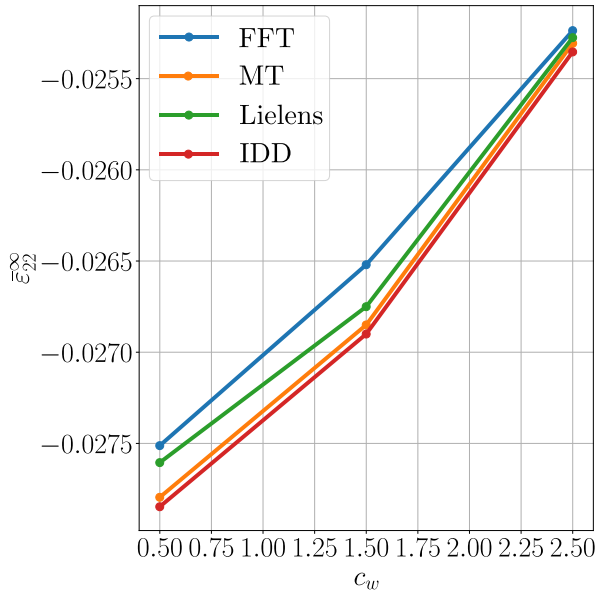
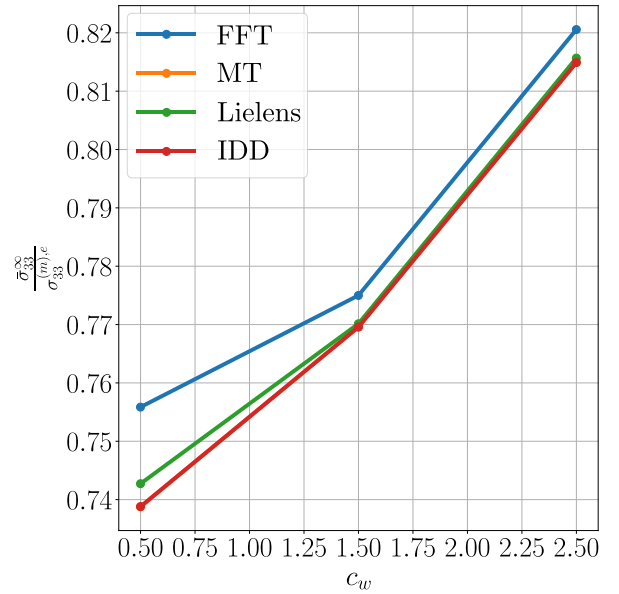

 (a) On-plane residual strain ( $\epsilon_{11}$ ).

 (b) Filament axis residual stress ( $\sigma_{33}$ ).

**Figure 22:** Strain and normalized stress response vs. temperature ( $T$ ), computed for load case 3,  $c^{(f)} = 0.2$ ,  $m_{AT} = 10$ ,  $c_w = 1.5$  and  $w_0 = 30$ .

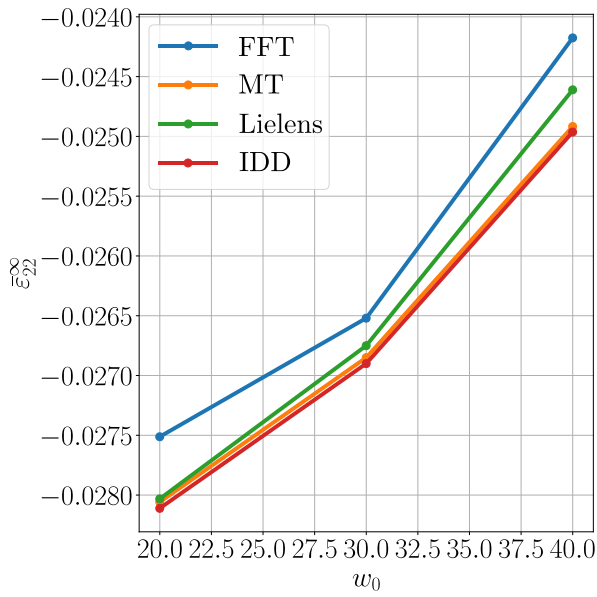
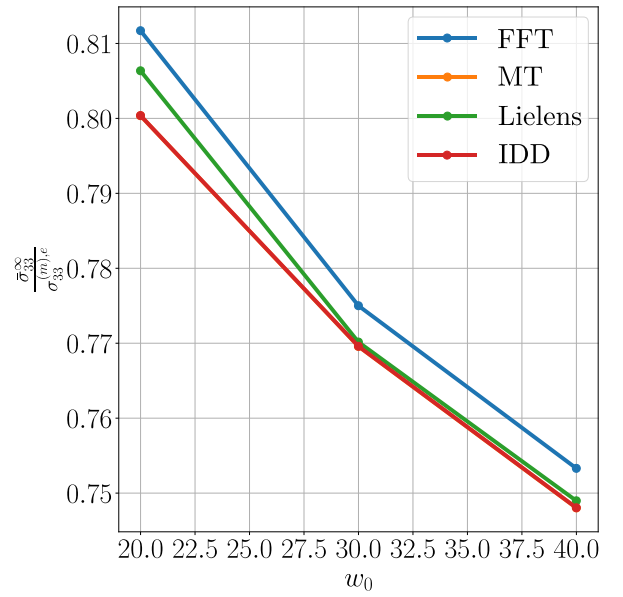

 (a) On-plane residual strain ( $\epsilon_{11}$ ).

 (b) Filament axis residual stress ( $\sigma_{33}$ ).

**Figure 23:** Asymptotic strain and normalized stress response vs. the volume fraction ( $c^{(f)}$ ), computed for load case 3, Cooling time = 8.64[s],  $m_{AT} = 10$ ,  $c_w = 1.5$  and  $w_0 = 30$ .


 (a) On-plane residual strain ( $\epsilon_{11}$ ).

 (b) Filament axis residual stress ( $\sigma_{33}$ ).

**Figure 24:** Asymptotic strain and normalized stress response vs. the Advani-Tucker parameter  $m_{AT}$ , computed for load case 3, Cooling time = 8.64[s],  $c^{(f)} = 0.2$ ,  $c_w = 1.5$  and  $w_0 = 30$ .

 (a) On-plane residual strain ( $\epsilon_{11}$ ).

 (b) Filament axis residual stress ( $\sigma_{33}$ ).

**Figure 25:** Asymptotic strain and normalized stress response vs. the Weibull's parameter  $c_w$ , computed for load case 3, Cooling time = 8.64[s],  $c^{(f)} = 0.2$ ,  $m_{AT} = 10$  and  $w_0 = 30$ .


 (a) On-plane residual strain ( $\epsilon_{11}$ ).

 (b) Filament axis residual stress ( $\sigma_{33}$ ).

**Figure 26:** Asymptotic strain and normalized stress response vs. the Weibull's parameter  $w_0$ , computed for load case 3, Cooling time = 8.64[s],  $c^{(f)} = 0.2$ ,  $m_{AT} = 10$  and  $c_w = 1.5$ .

## 5. Conclusions & Perspectives

As it was shown in the simulations section, the proposed procedure to compute the effective macroscopic behavior of an SPC filament exhibits a remarkable accuracy compared to the full-field simulations for all the different REV's that were tested. In addition, this fact confirms the validity of the probabilistic description of the fibers' microstructural parameters (i.e. length and orientation). This procedure holds consistency when computing the mechanical response (stress or strain) when different mechanical constraints are applied. The accuracy of the procedure was verified when different cooling rates are applied in the thermal history, then confirming the good agreement when considering the instantaneous or delayed components of the macroscopic mechanical responses. The highlights of the proposed methodology are:

- Polymer matrix representation that holds thermodynamic consistency; being able to map the delayed response in terms of volume variations in function of temperature, reproducing the transitional states from rubbery to glassy behavior. This fact is indeed of primal importance, as the nature of the manufacturing process imposes the thermal strain as the main source of residual stress and dimensional instability in an HT-FRAM 3D-printed composite part.
- Concise methodology, constructed around practical and functional choices, giving to the formulation simplicity while conserving its reliability, reducing dramatically the time of computations when comparing to full-field analysis (Table. 2). This is achieved through the introduction of the extension of analytical homogenization in the context of thermo-viscoelasticity via the internal-time technique for the correspondence principle in continuous variations of temperature, and ensuring the mathematical representation of the composite in the same way as the matrix by introducing an identification step, able to identify optimal values of the discrete spectra when no noisy data is used.
- Efficient implementation of the estimation of the influence of the variability of length and orientations in the effective behavior by implementing probabilistic descriptions of the parameters' distributions. Giving a plus in simplicity of formulation while being a more accurate description of the general state of the composite.
- High accurate Methodology to approximate effective thermo-viscoelastic behavior in discontinuous-fiber reinforced amorphous polymers, with high capacity of adaptation in finite elements commercial software products, as it has already been tested (Abaqus and Digimat).

In terms of perspectives, the next step will be to model the effective thermo-viscoelastic behavior of the printed part at the upper scale with the porosities due to the stacking of the filaments (mesoscale) by integrating the effective behavior model of the composite filament proposed in this paper and the topology of the porosities to solve the thermomechanical structure calculation in order to predict the warping of the HT FRAM 3D-printed part and to compare against experiments performed in simple structures.

## Acknowledgments

This study was supported in part by the SPRING project through a postdoctoral fellow-ship at the laboratory of mechanics and acoustics of Marseille (LMA).



## A. Mean-field models

Here, the explicit forms of the localization tensors  $\mathbf{A}_\star^{*(f)}$  used in the computation of its distribution averaged form  $\mathbf{A}_\star^{*(f)}$  after Eqs. (17)-(20), are presented. Recalling the explicit form of the latter:

$$\mathbf{A}_\star^{*(f)} = \int_S \int_{w_{\min}}^{w_{\max}} f_w(w) f_n(\mathbf{n}) \mathbf{A}^{(r)}(w, \mathbf{n}) dw dS \quad (\text{A.1})$$

*Localization tensors for the implemented mean-field schemes:*

All mean-fields approximations are based on Eshelby's equivalent inclusion method, whose results and notations are summarized. Consider an ellipsoidal domain  $\Omega^{(r)}$  embedded in an infinite matrix with elastic tensor  $\mathbf{L}^{(m)}$ , supporting a constant internal stress (or *polarization*)  $\boldsymbol{\tau}$  so that the total stress is  $\boldsymbol{\sigma}^{(r)} = \mathbf{L}^{(m)} : \boldsymbol{\epsilon}^{(r)} + \boldsymbol{\tau}$ , where  $\boldsymbol{\epsilon}^{(r)}$  is the total strain inside the inclusion. Then this strain is found to be constant and equal to:

$$\boldsymbol{\epsilon}^{(r)} = -\mathbf{P}_0^{(r)} : \boldsymbol{\tau} \quad (\text{A.2})$$

where  $\mathbf{P}_0^{(r)}$  is *Hill's tensor*, and depends on the matrix moduli and the inclusion's shape. Now consider that the domain  $\Omega^{(r)}$  supports an *inhomogeneity* characterized by the elastic tensor  $\mathbf{L}^{(r)}$ , and is submitted to a strain field  $\boldsymbol{\epsilon}_0$  uniform at infinity. Then, writing  $\boldsymbol{\sigma}^{(r)} = \mathbf{L}^{(r)} : \boldsymbol{\epsilon}^{(r)} = \mathbf{L}^{(m)} : \boldsymbol{\epsilon}^{(r)} + (\mathbf{L}^{(r)} - \mathbf{L}^{(m)}) : \boldsymbol{\epsilon}^{(r)}$ , i.e. introducing the polarization  $\boldsymbol{\tau} = (\mathbf{L}^{(r)} - \mathbf{L}^{(m)}) : \boldsymbol{\epsilon}^{(r)}$ , applying the previous formula (A.2) one obtains by superposition

$$\boldsymbol{\epsilon}^{(r)} = \boldsymbol{\epsilon}_0 - \mathbf{P}_0^{(r)} : (\mathbf{L}^{(r)} - \mathbf{L}^{(m)}) : \boldsymbol{\epsilon}^{(r)} \quad (\text{A.3})$$

and finally,

$$\boldsymbol{\epsilon}^{(r)} = \mathbf{A}_0^{(r)} : \boldsymbol{\epsilon}_0, \quad \mathbf{A}_0^{(r)} = \left[ \mathbf{I}_4 + \mathbf{P}_0^{(r)} : (\mathbf{L}^{(r)} - \mathbf{L}^{(m)}) \right]^{-1}. \quad (\text{A.4})$$

where  $\mathbf{A}_0^{(r)}$  is the *localization tensor* of the inclusion  $\Omega^{(r)}$  embedded in the matrix  $\mathbf{L}_0$ . Both Hill and localization tensors' expressions are given in [51] for a wide variety of inclusion shapes. The localization tensor  $\mathbf{A}_0^{(r)}$  is used in the dilute approximation, or Eshelby's model, valid only for very low volume fractions of inclusions where interactions between inclusions are negligible. For higher volume fractions, these interactions must be accounted for, as proposed by various authors.

*Mori–Tanaka (MT) model:* As reformulated by [4], in this model the mean inclusion strain is linked to the mean matrix strain (rather than the total mean strain) through Eshelby's method. This results in the following localization tensor:

$$\mathbf{A}_{\text{MT}}^{(r)} = \mathbf{A}_0^{(r)} : \left[ \left( 1 - \sum_{r=2}^R c^{(r)} \right) \mathbf{I}_4 + \sum_{r=2}^R c^{(r)} \mathbf{A}_0^{(r)} \right]^{-1}, \quad (\text{A.5})$$

where  $c^{(r)}$  is the inclusion's volume fraction.

*Lielens' model:* This model, introduced in [39], results from an interpolation between two bounds of the effective properties: (i) the lower Hashin and Shtrikman bound (corresponding to the MT model), and (ii) an upper bound, obtained by inverting the properties and geometries of matrix and fibers. The resulting localization tensor is:

$$\mathbf{A}_{\text{Lie}}^{(r)} = \overline{\mathbf{A}}^{(r)} : \left[ \left( 1 - \sum_{r=2}^R c^{(r)} \right) \mathbf{I}_4 + \sum_{r=2}^R c^{(r)} \overline{\mathbf{A}}^{(r)} \right]^{-1}, \quad \text{where } \overline{\mathbf{A}}^{(r)} = \left[ (1 - \eta_L) \left[ \mathbf{A}_0^{(r)} \right]^{-1} + \eta_L \left[ \mathbf{A}_{\text{inv}}^{(r)} \right]^{-1} \right]^{-1}, \quad (\text{A.6})$$

where  $\mathbf{A}_{\text{inv}}^{(r)}$  is the tensor given by Eq. (A.4) by inverting the matrix' and inclusion properties, and  $\eta_L$  being the interpolation factor depending on the volume fraction. Lielens proposes to use:

$$\eta_L = \frac{1}{2} c^{(r)} (1 + c^{(r)}), \quad (\text{A.7})$$

a choice that was validated by subsequent studies.

*Interaction direct derivative (IDD) model:* This model, introduced by [19, 63], comes from a double inclusion approach whereas a micromechanical analysis is performed by considering a matrix cell  $\Omega_D^{(r)}$  of ellipsoidal geometry surrounding each inclusion  $\Omega^{(r)}$ , itself surrounded by the effective medium. After some simplifications, the resulting concentration tensor for an inclusion is:

$$\mathbf{A}_{\text{IDD}}^{(r)} = \mathbf{A}_0^{(r)} : \left[ \mathbf{I}_4 - \sum_{r=2}^R c^{(r)} \mathbf{P}_0^{(\text{D},r)} : (\mathbf{L}^{(r)} - \mathbf{L}^{(\text{m})}) : \mathbf{A}_0^{(r)} \right]^{-1}, \quad (\text{A.8})$$

As pointed out by [19] and recently recalled by [27], the IDD model is in fact a general formulation that embeds (i) the MT model when each cell has the same geometry as its related inclusion (i.e.  $\mathbf{P}_0^{(\text{D},r)} = \mathbf{P}_0^{(r)}$ ), and (ii) the Ponte-Castañeda and Willis (PCW) model from [10] when all cells are identical and their shape characterizes the distribution of inclusions' centers (i.e.  $\mathbf{P}_0^{(\text{D},r)} = \mathbf{P}_0^{(\text{D})}$ ).

## B. Mathematical tools

### B.1. Transversely isotropic elasticity tensors and matrix representation

The explicit form of the Hill basis tensors for a given symmetry axis orientation ( $\mathbf{n}$ ) is presented below.

$$\begin{aligned}\mathcal{N} &= \mathbf{n} \otimes \mathbf{n}, \quad \Theta = \mathbf{I}_2 - \mathcal{N}, \\ \mathcal{H}^{(1)}(\mathbf{n}) &= \frac{1}{2} \Theta \otimes \Theta, \quad \mathcal{H}^{(2)}(\mathbf{n}) = \Theta \otimes \mathcal{N}, \quad \mathcal{H}^{(3)}(\mathbf{n}) = \mathcal{N} \otimes \Theta, \quad \mathcal{H}^{(4)}(\mathbf{n}) = \mathcal{N} \otimes \mathcal{N}, \\ \mathcal{H}^{(5)}(\mathbf{n}) &= \frac{1}{2} (\Theta_{ik} \Theta_{lj} + \Theta_{il} \Theta_{kj} - \Theta_{ij} \Theta_{kl}), \\ \mathcal{H}^{(6)}(\mathbf{n}) &= \frac{1}{2} (\Theta_{ik} \mathcal{N}_{lj} + \Theta_{il} \mathcal{N}_{kj} + \Theta_{jk} \mathcal{N}_{li} + \Theta_{jl} \mathcal{N}_{ki}).\end{aligned}\tag{B.1}$$

With  $\otimes$  representing the tensor product.

Transversely isotropic elasticity tensors are written in Hill basis as:

$$\mathbf{L} = 2K\mathcal{H}^1 + \ell(\mathcal{H}^2 + \mathcal{H}^3) + n\mathcal{H}^4 + 2m\mathcal{H}^5 + 2\mu\mathcal{H}^6 = \sum_{b=1}^6 l^{(b)} \mathcal{H}^{(b)},\tag{B.2}$$

where:

- $K$  is the plane strain bulk modulus.
- $m$  is the transverse shear modulus: ( $m = G_{23}$  if  $\mathbf{n} = \mathbf{e}_1$ ).
- $\mu$  is the longitudinal shear modulus: ( $\mu = G_{12} = G_{13}$  if  $\mathbf{n} = \mathbf{e}_1$ ).
- $\ell$  and  $n$  can be linked to the “engineering” constants, e.g if  $\mathbf{n} = \mathbf{e}_1$ :

$$\ell/2K = \nu_{12}, \quad n - \ell^2/K = E_1.\tag{B.3}$$

In  $6 \times 6$  matrix representation (Voigt notations), taking  $\mathbf{n} = \mathbf{e}_1$ , one has [2]

$$\mathbf{L}_{\text{Voigt}} = \begin{bmatrix} L_{11} & L_{12} & L_{12} & 0 & 0 & 0 \\ L_{12} & L_{22} & L_{23} & 0 & 0 & 0 \\ L_{12} & L_{23} & L_{22} & 0 & 0 & 0 \\ 0 & 0 & 0 & (L_{22} - L_{23})/2 & 0 & 0 \\ 0 & 0 & 0 & 0 & L_{55} & 0 \\ 0 & 0 & 0 & 0 & 0 & L_{55} \end{bmatrix} = \begin{bmatrix} n & \ell & \ell & 0 & 0 & 0 \\ \ell & K+m & K-m & 0 & 0 & 0 \\ \ell & K-m & K+m & 0 & 0 & 0 \\ 0 & 0 & 0 & m & 0 & 0 \\ 0 & 0 & 0 & 0 & \mu & 0 \\ 0 & 0 & 0 & 0 & 0 & \mu \end{bmatrix}.\tag{B.4}$$

Using “engineering” coefficients (e.g. ( $E_1, E_2, \nu_{12}, G_{12}, G_{23}$ )) the associated compliance matrix is:

$$\mathbf{S}_{\text{Voigt}} = \begin{bmatrix} \frac{1}{E_1} & -\frac{\nu_{12}}{E_2} & -\frac{\nu_{12}}{E_2} & 0 & 0 & 0 \\ -\frac{\nu_{21}}{E_1} & \frac{1}{E_2} & -\frac{\nu_{32}}{E_2} & 0 & 0 & 0 \\ -\frac{\nu_{21}}{E_1} & -\frac{\nu_{32}}{E_2} & \frac{1}{E_2} & 0 & 0 & 0 \\ 0 & 0 & 0 & \frac{1}{G_{23}} & 0 & 0 \\ 0 & 0 & 0 & 0 & \frac{1}{G_{12}} & 0 \\ 0 & 0 & 0 & 0 & 0 & \frac{1}{G_{12}} \end{bmatrix},\tag{B.5}$$

where  $\nu_{21}$  is determined by the symmetry requirement  $\nu_{21}/E_1 = \nu_{12}/E_2$ .

Double product “.”	$\mathcal{N}$	$\Theta$
$\mathcal{H}^{(1)}$	$\mathbf{0}$	$\Theta$
$\mathcal{H}^{(2)}$	$\Theta$	$\mathbf{0}$
$\mathcal{H}^{(3)}$	$\mathbf{0}$	$2\mathcal{N}$
$\mathcal{H}^{(4)}$	$\mathcal{N}$	$\mathbf{0}$
$\mathcal{H}^{(5)}$	$\mathbf{0}$	$\mathbf{0}$
$\mathcal{H}^{(6)}$	$\mathbf{0}$	$\mathbf{0}$

**Table 4**

Product between fourth-order Hill basis tensor and second-order tensor of the natural basis of transverse isotropic tensors.

For completely isotropic materials, one has:

$$\mathbf{L}_{\text{Voigt}} = \begin{bmatrix} \lambda + 2\mu & \lambda & \lambda & 0 & 0 & 0 \\ \lambda & \lambda + 2\mu & \lambda & 0 & 0 & 0 \\ \lambda & \lambda & \lambda + 2\mu & 0 & 0 & 0 \\ 0 & 0 & 0 & \mu & 0 & 0 \\ 0 & 0 & 0 & 0 & \mu & 0 \\ 0 & 0 & 0 & 0 & 0 & \mu \end{bmatrix}, \quad \text{so that} \quad \begin{cases} K = \lambda + \mu & = \kappa + \frac{1}{3}\mu \\ \ell = \lambda & = \kappa - \frac{2}{3}\mu \\ n = \lambda + 2\mu & = \kappa + \frac{4}{3}\mu \\ m = \mu \end{cases} \quad (\text{B.6})$$

where we used  $\lambda = \kappa - 2\mu/3$ .

## B.2. Products of tensors in Hill basis

By Table. 4, the product between fourth- and second-order transverse isotropic tensors is:

$$\mathbf{T} : \mathbf{t} = (T_4 t_1 + 2T_3 t_2)\mathcal{N} + (T_2 t_1 + T_1 t_2)\Theta. \quad (\text{B.7})$$

## B.3. Orientation averaged Hill basis

By Eq. (B.1) it is noted that the orientation averaging of the Hill basis is reduced to the computation of the second and fourth order orientation tensors, interpreted as the second and fourth order moments of the orientation distribution respectively [1]. the expressions of the orientation tensors are presented below.

$$\eta_2 = \int_S f_n(\mathbf{n})(\mathbf{n} \otimes \mathbf{n})dS, \quad \eta_4 = \int_S f_n(\mathbf{n})(\mathbf{n} \otimes \mathbf{n} \otimes \mathbf{n} \otimes \mathbf{n})dS. \quad (\text{B.8})$$

The explicit forms of the orientation averaged Hill basis reads

$$\begin{aligned} \mathcal{H}_\star^{(1)} &= \frac{1}{2} [I_2 \otimes I_2 - I_2 \otimes \eta_2 - \eta_2 \otimes I_2 + \eta_4], \quad \mathcal{H}_\star^{(2)} = I_2 \otimes \eta_2 - \eta_4, \quad \mathcal{H}_\star^{(3)} = \eta_2 \otimes I_2 - \eta_4 \\ \mathcal{H}_\star^{(4)} &= \eta_4, \quad \mathcal{H}_\star^{(5)} = \frac{1}{2} [2I_4 - \lambda - I_2 \otimes \eta_2 + I_2 \otimes \eta_2 + \eta_2 \otimes I_2 + \eta_4], \quad \mathcal{H}_\star^{(6)} = \frac{1}{2} \lambda - 2\eta_4 \\ \lambda_{ijkl} &= (I_2)_{ik}(\eta_2)_{jl} + (\eta_2)_{ik}(I_2)_{jl} + (I_2)_{il}(\eta_2)_{jk} + (\eta_2)_{il}(I_2)_{jk}. \end{aligned} \quad (\text{B.9})$$

## B.4. Orientation tensors for Advani-Tucker law

By Eq. B.8, the orientation tensors in matrix notation corresponding to the Advani-Tucker law for the axisymmetric distribution, can be computed as follows:

$$\begin{aligned} \eta_2 &= \frac{1}{m_{\text{AT}} + 3} \begin{bmatrix} m_{\text{AT}} + 1 & 0 & 0 \\ 0 & 1 & 0 \\ 0 & 0 & 1 \end{bmatrix} \\ \eta_4 &= \frac{1}{(m_{\text{AT}} + 3)(m_{\text{AT}} + 5)} \begin{bmatrix} (m_{\text{AT}} + 1)(m_{\text{AT}} + 3) & (m_{\text{AT}} + 1) & (m_{\text{AT}} + 1) & 0 & 0 & 0 \\ (m_{\text{AT}} + 1) & 3 & 1 & 0 & 0 & 0 \\ (m_{\text{AT}} + 1) & 1 & 3 & 0 & 0 & 0 \\ 0 & 0 & 0 & 1 & 0 & 0 \\ 0 & 0 & 0 & 0 & (m_{\text{AT}} + 1) & 0 \\ 0 & 0 & 0 & 0 & 0 & (m_{\text{AT}} + 1) \end{bmatrix} \end{aligned} \quad (\text{B.10})$$

### C. Parameters identification

The Laplace-Carson transform of a relaxation moduli tensor  $\mathbf{L}^*$ , gives the steady-state response to a harmonic loading by considering the change of variable  $p = j\omega$ , with  $\omega$  being the circular velocity of the harmonic loading [25, 21]. This is why identification methods developed for this kind of harmonic loading (e.g. DMA tests) are implemented to estimate the coefficients of an equivalent Prony-series representing the effective thermo-viscoelastic behavior from the generated data.

Let  $m(t)$  be a given relaxation modulus (an element of  $\mathbf{L}(t)$ ), and  $m^*(p)$  its correspondent Laplace-Carson transform. The identification of the coefficients of  $m(t)$  begins with the approximation of the discrete characteristic time distribution. This is achieved by using the Krein-Nudelman method [30]. After this, the associated coefficients are computed from a classic mean-squares procedure. The methodology to approximate Prony-series is presented as follows:

Given the frequency data:  $\{\omega_i, \hat{m}_i\}$ , with  $m_i^* = m'_i + jm''_i$ , and its conjugate form  $\hat{m}_i$ , with  $i \in [1, I]$ . Find an approximation for  $\tau_n$ ,  $N_\tau$  and  $m_n$ , that are the discrete time distribution and its size, and the coefficients associated to each characteristic time, respectively:

- Build the following square matrices:

$$\mathbf{M}_{kl}^1 = j \frac{\hat{m}_k - m_l^*}{\omega_k + \omega_l}, \quad \mathbf{M}_{kl}^2 = \frac{\hat{m}_k + m_l^*}{\omega_k + \omega_l}. \quad (\text{C.1})$$

- Compute the eigenvectors  $\lambda^1$  and  $\lambda^2$  associated to the null space of  $\mathbf{M}^1$  and  $\mathbf{M}^2$ , then compute the following two functions:

$$f_1(s) = \sum_{i=1}^I \frac{\lambda_i^1}{s + j\omega_i}, \quad f_2(s) = \sum_{i=1}^I \frac{\lambda_i^2}{s + j\omega_i}. \quad (\text{C.2})$$

- Discretize  $f_1$  and  $f_2$  considering  $s$  as a frequency variable lying in the same range of  $\{\omega_i/2\pi\}$ . Then, find numerically the common real positive zeros ( $s_n$ ) corresponding to the discrete characteristic times of the relaxation modulus  $m(t)$ :

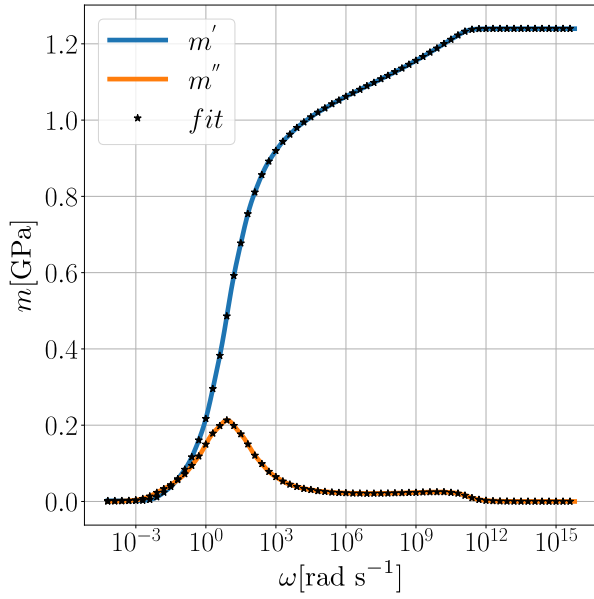
$$\tau_n = (s_n)^{-1}, \quad n \in [1, N_\tau] \quad (\text{C.3})$$

- Build the following rectangular matrices:

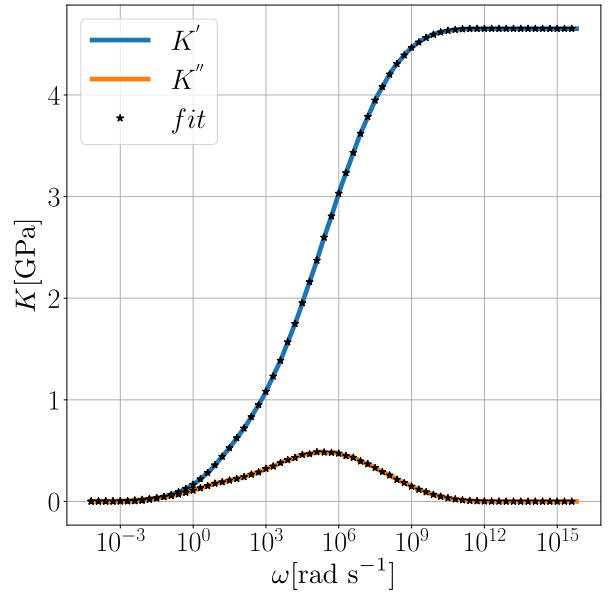
$$\mathbf{A}_{in}^1 = \frac{(\omega_i \tau_n)^2}{1 + (\omega_i \tau_n)^2}, \quad \mathbf{A}_{in}^2 = \frac{\omega_i \tau_n}{1 + (\omega_i \tau_n)^2} \quad (\text{C.4})$$

- The associated moduli are computed by solving the following minimization problem:

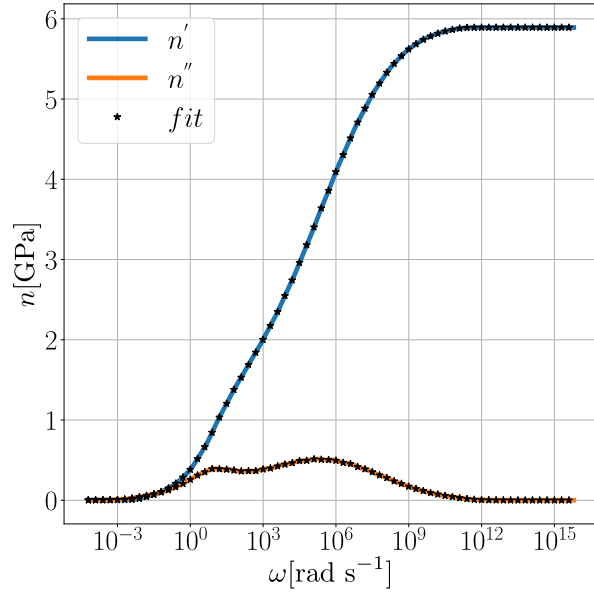
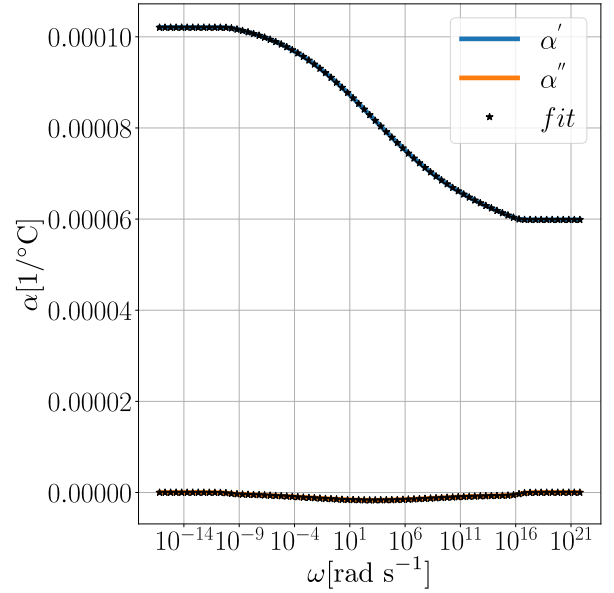
$$\{m_n\} = \operatorname{argmin} (||\mathbf{A}^1 \cdot \{m_n\} - \{m'_i\}|| + ||\mathbf{A}^2 \cdot \{m_n\} - \{m''_i\}||) \quad (\text{C.5})$$



(a) On-plane shear relaxation modulus.



(b) On-plane compressibility relaxation modulus.


 (c) relaxation modulus related with the axial behavior  $n$ .


(d) On-plane thermal creep function.

Figure 27: Identification examples using Krein-Nudelmann method.

## D. Materials' data

Fibers' mechanical properties are assumed to be constant:  $\kappa = 39.733[\text{GPa}]$ ,  $\mu = 29.05[\text{GPa}]$  and  $\alpha = 2.21\text{E} - 5[1/^\circ\text{C}]$ .

Matrix coefficients for the reference master-curves are presented below:

Glassy moduli:  $\kappa_g = 4.23879[\text{GPa}]$ ,  $\mu_g = 1.23968[\text{GPa}]$

$\tau^{(u)}[\text{s}]$	$\kappa^{(u)}[\text{GPa}]$	$\mu^{(u)}[\text{GPa}]$
1.4211E - 11	0.0284181	0.0284181
7.2697E - 11	0.0341941	0.0273223
3.7188E - 10	0.0920182	0.0255737
1.9024E - 9	0.172648	0.0237469
9.7315E - 9	0.268286	0.0222851
4.9782E - 8	0.366893	0.0214578
2.5466E - 7	0.452075	0.0214489
1.3027E - 6	0.505714	0.0224768
6.6640E - 6	0.514237	0.0249357
3.4089E - 5	0.47587	0.0296341
1.7439E - 4	0.402704	0.0383457
8.9208E - 4	0.314523	0.055318
4.5634E - 3	0.229389	0.0917189
0.0233442	0.158053	0.174055
0.119418	0.103904	0.274284
0.610883	0.0656627	0.187685
3.12498	0.040106	0.0904041
15.9858	0.0237646	0.0485919
81.7757	0.0136966	0.0302413

Glassy modulus:  $\alpha_g = 5.98536\text{E} - 5[1/^\circ\text{C}]$

$\tau^{(s)}[\text{s}]$	$\alpha^{(s)}[1/^\circ\text{C}]$	$\tau^{(s)}[\text{s}]$	$\alpha^{(s)}[1/^\circ\text{C}]$
1.09402E - 16	6.43788E - 7	1.48477E - 3	1.63691E - 6
4.96202E - 16	6.54383E - 7	6.73427E - 3	1.62182E - 6
2.25056E - 15	6.74554E - 7	3.05438E - 2	1.59023E - 6
1.02075E - 14	7.03568E - 7	1.38533E - 1	1.54303E - 6
4.62970E - 14	7.40899E - 7	6.28327E - 1	1.48174E - 6
2.09983E - 13	7.86106E - 7	2.84982	1.40840E - 6
9.52393E - 13	8.38741E - 7	12.9255	1.32544E - 6
4.31964E - 12	8.98259E - 7	58.6247	1.23550E - 6
1.95920E - 11	9.63950E - 7	265.896	1.14129E - 6
8.88601E - 11	1.03487E - 6	1205.99	1.04541E - 6
4.03035E - 10	1.10980E - 6	5469.85	9.50225E - 7
1.82799E - 9	1.18721E - 6	24808.9	8.57797E - 7
8.29098E - 9	1.26525E - 6	112522	7.69789E - 7
3.76043E - 8	1.34181E - 6	510353	6.87463E - 7
1.70557E - 7	1.41451E - 6	2.31474E + 6	6.11684E - 7
7.73572E - 7	1.48087E - 6	1.04987E + 7	5.42952E - 7
3.50859E - 6	1.53837E - 6	4.76174E + 7	4.81461E - 7
1.59134E - 5	1.58461E - 6	2.15972E + 8	4.27147E - 7
7.21765E - 5	1.61749E - 6	9.79554E + 8	3.79766E - 7
3.27361E - 4	1.63530E - 6	4.44283E + 9	3.38943E - 7



## References

- [1] Advani, S.G., Tucker, C.L., 1987. The use of tensors to describe and predict fiber orientation in short fiber composites. *J. Rheol.* 31, 751–784.
- [2] Afidi, J.C.H., Kardos, J.L., 1976. The halpin-tsai equations: A review. *Polym. Eng.* 16, 344–352.
- [3] Andrews, R.D., Tobolsky, A.V., 1951. Elastoviscous properties of polyisobutylene. iv. relaxation time spectrum and calculation of bulk viscosity. *J. Polym. Sci.* 7, 221–242.
- [4] Benveniste, Y., 1987. A new approach to the application of mori-tanaka's theory in composite materials. *Mech. Mater.* 6, 147–157.
- [5] Biot, M.A., 1965. Mechanics of incremental deformations. *Wiley*.
- [6] Bornert, M., Bretheau, T., Gilormini, P., 2001. Homogénéisation en mécanique des matériaux, Tome 1 : Matériaux aléatoires élastiques et milieux périodiques. Hermes science.
- [7] Brassart, L., Stainier, L., Doghri, I., Delannay, L., 2012. Homogenization of elasto-(visco) plastic composites based on an incremental variational principle. *Int. J. Plast.* 36, 86–112.
- [8] Burgarella, B., Maurel-Pantel, A., Lahellec, N., Bouvard, J.L., Billon, N., 2020. Modeling the effective viscoelastic properties of peek matrix reinforced by arbitrary oriented short glass fibers. *Mech. Time Depend. Mater.* , 1–29.
- [9] Burgarella, B., Maurel-Pantel, A., Lahellec, N., Bouvard, J.L., Billon, N., Moulinec, H., Lebon, F., 2019. Effective viscoelastic behavior of short fibers composites using virtual dma experiments. *Mech. Time Depend. Mater.* 23, 337–360.
- [10] Castañeda, P., Willis, J., 1995. The effect of spatial distribution on the effective behavior of composite materials and cracked media. *J. Mech. Phys.* 43, 1919–1951.
- [11] Chen, G., Wang, D., Hua, W., Wu, W., Zhou, W., Jin, Y., Zheng, W., 2021. Simulating and predicting the part warping in fused deposition modeling by thermal-structural coupling analysis. *3D Print. Addit. Manuf.* .
- [12] Chen, X., Nguyen, T.D., 2011. Influence of thermoviscoelastic properties and loading conditions on the recovery performance of shape memory polymers. *Mech. Mater.* 43, 127 – 138.
- [13] Christensen, R.M., 1982. Theory of viscoelasticity. Dover Publications Inc.
- [14] Crochet, M.J., Naghdi, P.M., 1970. On 'thermo-rheologically simple' solids, in: Boley, B.A. (Ed.), *Thermoinelasticity*, Springer Vienna, Vienna. pp. 59–86.
- [15] Das, A., Chatham, C.A., Fallon, J.J., Zawaski, C.E., Gilmer, E.L., Williams, C.B., Bortner, M.J., 2020. Current understanding and challenges in high temperature additive manufacturing of engineering thermoplastic polymers. *Additive Manufacturing* 34, 101218.
- [16] Despringre, N., Chemisky, Y., Bonnay, K., Meraghni, F., 2016. Micromechanical modeling of damage and load transfer in particulate composites with partially debonded interface. *Compos. Struct.* 155, 77–88.
- [17] Dirrenberger, J., Forest, S., Jeulin, D., 2014. Towards gigantic RVE sizes for 3d stochastic fibrous networks. *Int. J Solids Struct.* 51, 359–376.
- [18] Dizon, J.R.C., Espera, A.H., Chen, Q., Advincula, R.C., 2018. Mechanical characterization of 3d-printed polymers. *Addit. Manuf.* 20, 44–67.
- [19] Du, D.X., Zheng, Q.S., 2002. A further exploration of the interaction direct derivative (idd) estimate for the effective properties of multiphase composites taking into account inclusion distribution. *Acta Mech.* 157, 61–80.
- [20] Ferry, J.D., 1950. Mechanical properties of substances of high molecular weight. vi. dispersion in concentrated polymer solutions and its dependence on temperature and concentration. *J. Am. Chem. Soc.* 72, 3746–3752.
- [21] Gallican, V., Brenner, R., 2019. Homogenization estimates for the effective response of fractional viscoelastic particulate composites. *Contin. Mech. Thermodyn.* 31, 823–840.
- [22] Goh, G.D., Yap, Y.L., Agarwala, S., Yeong, W.Y., 2019. Recent progress in additive manufacturing of fiber reinforced polymer composite. *Adv. Mater. Technol.* 4, 1800271.
- [23] Gross, B., da Fonseca, E.L., 1953. Mathematical structure of the theories of viscoelasticity. *Actualités Scientifiques et Industrielles*.
- [24] Gupta, A., Hasanov, S., Fidan, I., Zhang, Z., 2021. Homogenized modeling approach for effective property prediction of 3d-printed short fibers reinforced polymer matrix composite material. *Int. J. Adv. Manuf.* , 1–18.
- [25] Gutierrez-Lemini, D., 2014. Engineering viscoelasticity. Springer.
- [26] Haleem, A., Javaid, M., Rab, S., 2020. Impact of additive manufacturing in different areas of industry 4.0. *Int. J. Logist. Syst. Manag.* 37, 239–251.
- [27] Hessman, P.A., Welschinger, F., Hornberger, K., Böhlke, T., 2021. On mean field homogenization schemes for short fiber reinforced composites: Unified formulation, application and benchmark. *Int. J. Solids. Struct.* 230-231, 111141.
- [28] DassaultSystèmes, 2021. 3ds simulia simulation pour la fabrication additive.
- [29] E-Xstream, 2021. Digimat software for additive manufacturing.
- [30] Jalocha, D., Constantinescu, A., Neviere, R., 2015. Revisiting the identification of generalized Maxwell models from experimental results. *Int J Solids Struct* 67-68, 169–181.
- [31] Kammoun, S., Doghri, I., Brassart, L., Delannay, L., 2015. Micromechanical modeling of the progressive failure in short glass–fiber reinforced thermoplastics – First Pseudo-Grain Damage model. *Compos. Part A Appl. Sci.* 73, 166–175.
- [32] Kasmí, S., Ginoux, G., Allaoui, S., Alix, S., 2021. Investigation of 3d printing strategy on the mechanical performance of coextruded continuous carbon fiber reinforced petg. *J. Appl. Polym. Sci.* 138, 50955.
- [33] Knauss, W.G., Emri, I., 1987. Volume change and the nonlinearly thermo-viscoelastic constitution of polymers. *Polym. Eng. Sci.* 27, 86–100.
- [34] Kovacs, A.J., Aklonis, J.J., Hutchinson, J.M., Ramos, A.R., . Isobaric volume and enthalpy recovery of glasses. ii a transparent multiparameter theory. *J. Polym. Sci. B Polym. Phys.* 34.
- [35] Lahellec, N., Suquet, P., 2013. Effective response and field statistics in elasto-plastic and elasto-viscoplastic composites under radial and non-radial loadings. *Int. J. Plast.* 42, 1–30.
- [36] Leaderman, H., 1943. Elastic and creep properties of filamentous materials and other high polymers. Textile Foundation, Washington, D.C , 175.
- [37] Lee, J.Y., An, J., Chua, C.K., 2017. Fundamentals and applications of 3d printing for novel materials. *Appl. Mater. Today.* 7, 120–133.
- [38] Levin, V., 1967. Thermal expansion coefficients of heterogeneous materials. *Mech. Solids.* 2, 58–61.

- [39] Lielens, G., Pirotte, P., Couniot, A., Dupret, F., Keunings, R., 1998. Prediction of thermo-mechanical properties for compression moulded composites. *Compos. - A: Appl. Sci. Manuf.* 29, 63–70. Selected Papers Presented at the Fourth International Conference on Flow Processes in Composite Material.
- [40] L  vesque, M., Gilchrist, M.D., Bouleau, N., Derrien, K., Baptiste, D., 2007. Numerical inversion of the Laplace–Carson transform applied to homogenization of randomly reinforced linear viscoelastic media. *Comput. Mech.* 40, 771–789.
- [41] Mandel, J., 1966. Cours de M  canique des milieux continus. Gauthier–Villars.
- [42] Masson, R., Zaoui, A., 1999. Self-consistent estimates for the rate-dependent elastoplastic behaviour of polycrystalline materials. *J Mech. Phys. Solids* 47, 1543–1568.
- [43] Milton, G.W., May 2002. The theory of composites. Cambridge University Press.
- [44] Moulinec, H., Suquet, P., 1994. A fast numerical method for computing the linear and nonlinear mechanical properties of composites. *Comptes rendus de l'Academie des sciences. Serie II, Mecanique, physique, chimie, astronomie* 318, 1417–1423.
- [45] Moulinec, H., Suquet, P., 1998. A numerical method for computing the overall response of nonlinear composites with complex microstructure. *Comput. Methods. Appl. Mech. Eng.* 157, 69–94.
- [46] Muliana, A.H., 2009. A micromechanical model for predicting thermal properties and thermo-viscoelastic responses of functionally graded materials. *Int. J Solids Struct.* 46, 1911–1924.
- [47] Nguyen, B.N., Bapanapalli, S.K., Holbery, J.D., Smith, M.T., Kunc, V., Frame, B.J., Phelps, J.H., Charles L. Tucker, I., 2008. Fiber length and orientation in long-fiber injection-molded thermoplastics — part i: Modeling of microstructure and elastic properties. *J. Compos. Mater.* 42, 1003–1029.
- [48] Nguyen, T.D., Yakacki, C.M., Brahmabhatt, P.D., Chambers, M.L., 2010. Modeling the relaxation mechanisms of amorphous shape memory polymers. *Adv. Mater.* 22, 3411–3423.
- [49] Parandoush, P., Lin, D., 2017. A review on additive manufacturing of polymer-fiber composites. *Compos. Struct.* 182, 36–53.
- [50] Parlevliet, P.P., Bersee, H.E., Beukers, A., 2006. Residual stresses in thermoplastic composites—a study of the literature—part i: Formation of residual stresses. *Compos. Part A Appl. Sci.* 37, 1847–1857.
- [51] Parnell, J.W., 2016. The Eshelby, Hill, moment and concentration tensors for ellipsoidal inhomogeneities in the newtonian potential problem and linear elastostatics. *J. Elast.* 125, 231–294.
- [52] Ricaud, J.M., Masson, R., 2009. Effective properties of linear viscoelastic heterogeneous media: Internal variables formulation and extension to ageing behaviours. *Int J Solids Struct* 46, 1599–1606.
- [53] Rosen, B., Hashin, Z., 1970. Effective thermal expansion coefficients and specific heats of composite materials. *Int. J. Eng. Sci.* 8, 157–173.
- [54] Rougier, Y., Stolz, C., Zaoui, A., 1993. Spectral analysis of linear viscoelastic inhomogeneous materials. *Comptes rendus de l'Acad  mie des sciences. S  rie II, M  canique, physique, chimie, astronomie* 316, 1517–1522.
- [55] SABIC, 2018. ULTEM<sup>TM</sup> Resin 1000 - Americas. [UL Prospector from UL LLC](#).
- [56] Salen  on, J., 2019. Viscoelastic modeling for structural analysis. Wiley.
- [57] Shanguan, Y., Chen, F., Jia, E., Lin, Y., Hu, J., Zheng, Q., 2017. New insight into time-temperature correlation for polymer relaxations ranging from secondary relaxation to terminal flow: Application of a universal and developed wlf equation. *Polymers* 9.
- [58] Sreejith, P., Kannan, K., Rajagopal, K., 2021. A thermodynamic framework for additive manufacturing, using amorphous polymers, capable of predicting residual stress, warpage and shrinkage. *Int. J. Eng. Sci.* 159, 103412.
- [59] Taylor, R.L., Pister, K.S., Goudreau, G.L., 1970. Thermomechanical analysis of viscoelastic solids. *Int. J. Numer. Methods. Eng.* 2, 45–59.
- [60] Wickramasinghe, S., Do, T., Tran, P., 2020. Fdm-based 3d printing of polymer and associated composite: A review on mechanical properties, defects and treatments. *Polymers* 12, 1529.
- [61] Willis, J., 1977. Bounds and self-consistent estimates for the overall properties of anisotropic composites. *J. Mech. Phys. Solids.* 25, 185–202.
- [62] Yu, Q., Fish, J., 2002. Multiscale asymptotic homogenization for multiphysics problems with multiple spatial and temporal scales: a coupled thermo-viscoelastic example problem. *Int. J. Solids Struct.* 39, 6429–6452.
- [63] Zheng, Q.S., Du, D.X., 2001. An explicit and universally applicable estimate for the effective properties of multiphase composites which accounts for inclusion distribution. *J. Mech. Phys.* 49, 2765–2788. The Jean-Paul Boehler Memorial Volume.